UNIVERSIY OF GRONINGEN

ASTRONOMY BACHELOR PROJECT

# The Cosmic Web: Anisotropic Inflow along Filaments

*Author*
Carmen R. Hoek

*Supervisor*
Prof. dr. Rien van de Weijgaert

July 3, 2020

# Abstract

Looking at the data from the NEXUS+ simulations we see many interesting patterns. We are taking a special interest in the nodes. Firstly we will look at surface density patterns at different distances from the center of the node. We make plots of the surface density projected on the sky. Next, we look at the radial component of the velocity field and the momentum field in order to determine inflow patterns around the nodes. We use spherical harmonics up to a degree of $l = 2$ to determine primary structures in the velocity field and momentum field.

# Acknowledgments

First of all, I would like to thank prof. Rien van de Weijgaert for his continuous help with this project and giving me the opportunity to do this. I would also like to thank Roi Kugul for his help with starting and using NEXUS and answering all my questions about it.

# Contents

# 1 Cosmic Web & Cosmic Migration

## 1.1 What is the Cosmic Web?

Looking at the universe we find a lot of different kinds of structures, each at bigger scales. We start from structures like our solar system and we grow further towards galaxies, like our Milky Way, then groups of galaxies like the local group, clusters, and super clusters, but where does structure end? We find a final scale of structure at the scale of super clusters and filaments, after that there seems no structure to be found anymore, a phenomenon which is called the End of Greatness (Kirshner, 2002).

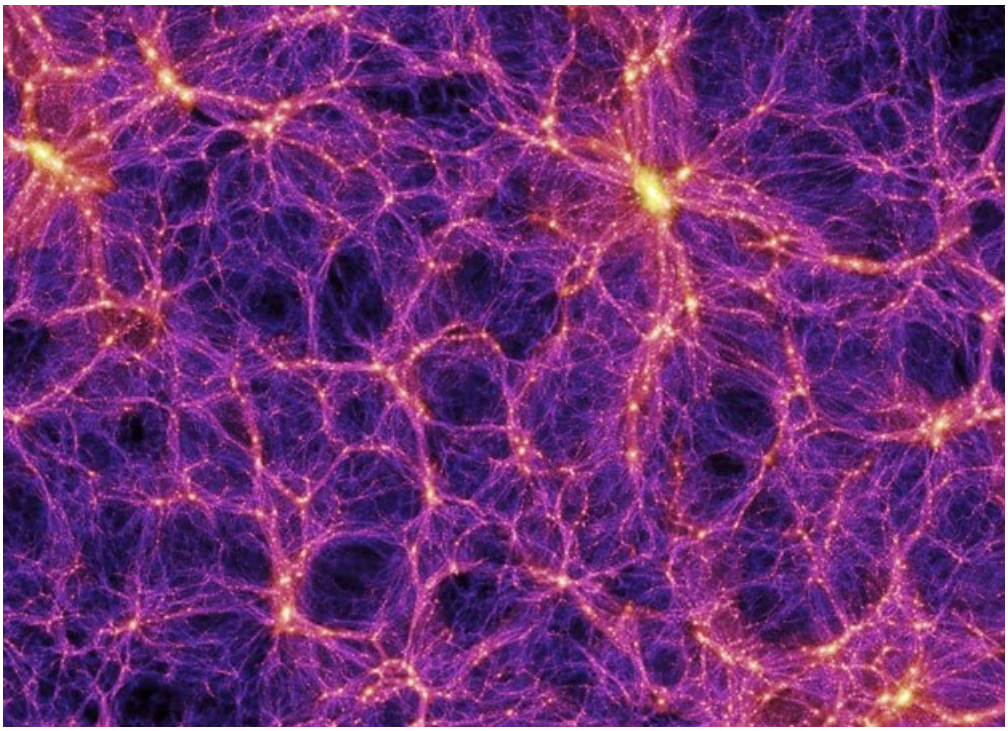

Figure 1: The Cosmic Web: Millennium simulation (Springel et al., 2005)

The Cosmic Web structure is the result of primordial density fluctuations quickly following the Big Bang. In order to describe the condensation of the gas, which starts the formation of structure, we need an approximation of the physical situation. In 1970, Zel'dovich published a paper showing that when you take an ellipsoid of gas on a cosmological scale, you can approximate the collapse of the region with a collapse happening along the short axis of the ellipsoid. If we assume that the collapse happens before the recombination era, we can approximate that the ellipsoid is large enough to set the pressure to zero and only consider the gravitational force. Thus implies that the gas will collapse without any significant influence of the perturbation of

the gas by outward pressure. This approximation is named after him and called the Zel'Dovich approximation (Zel'Dovich, 1970).

The Cosmic Web is this largest scale structure we can find, the scales range from 30 to 200 megaparsecs (Mpc) (Carroll and Ostlie, 2014). The name, Cosmic Web comes from the web-like structure we find at this scale created by a complex structure of filaments, nodes, walls, and voids. An example of these structures is found in figure 2. The mass and volume distribution between these structures is shown in figure 3. We will look at these terms in the next few sections.

## 1.2 Components of the Cosmic Web

### 1.2.1 Filaments

Filaments are the most outstanding features of the Cosmic Web, they form the spine of the entire structure. Even in the primordial density field, the proto-filaments formed a very important part of the primordial structure. When the non-linear evolution started, the filaments became even more present (Van de Weijgaert and Bond, 2005).

The elongated structures form the highways in the Cosmic Web structure, they connect high-density areas, like nodes, with each other and transport matter and galaxies between these regions (van Haarlem and van de Weygaert, 1993). The location of the filaments between the high-density regions make them look long and small, since they are constantly pulled towards the nodes in each direction. On average filaments have sizes between 10 megaparsec and 100 megaparsec (Bharadwaj, Bhavsar and Sheth, 2004).

The filaments are mostly consisting of dark matter, and the galaxies are located along this matter. The galaxies give us an impression of the distribution of dark matter since it is reasonable to assume that they follow a similar distribution. The filament are over dense regions. This implies that the gravitational attraction in these regions slows down the expansion of the space, causing them to expand slower than under-dense regions like voids (Van de Weijgaert and Bond, 2005).

We also find filaments in our local cosmic neighbourhood. The most prominent object is the Perseus-Pisces filament , connecting Lanaikea (the local super cluster) to the Perseus-Pisces super cluster. Other filaments in our local universe are found at scales from 10 megaparsec to 100 megaparsec, connecting super cluster such as the Great-Attractor (Lynden-Bell et al., 1988), the Shapley Region (Shapley, 1930) (Proust et al., 2006) and the Vela super cluster (Courtois et al., 2019).

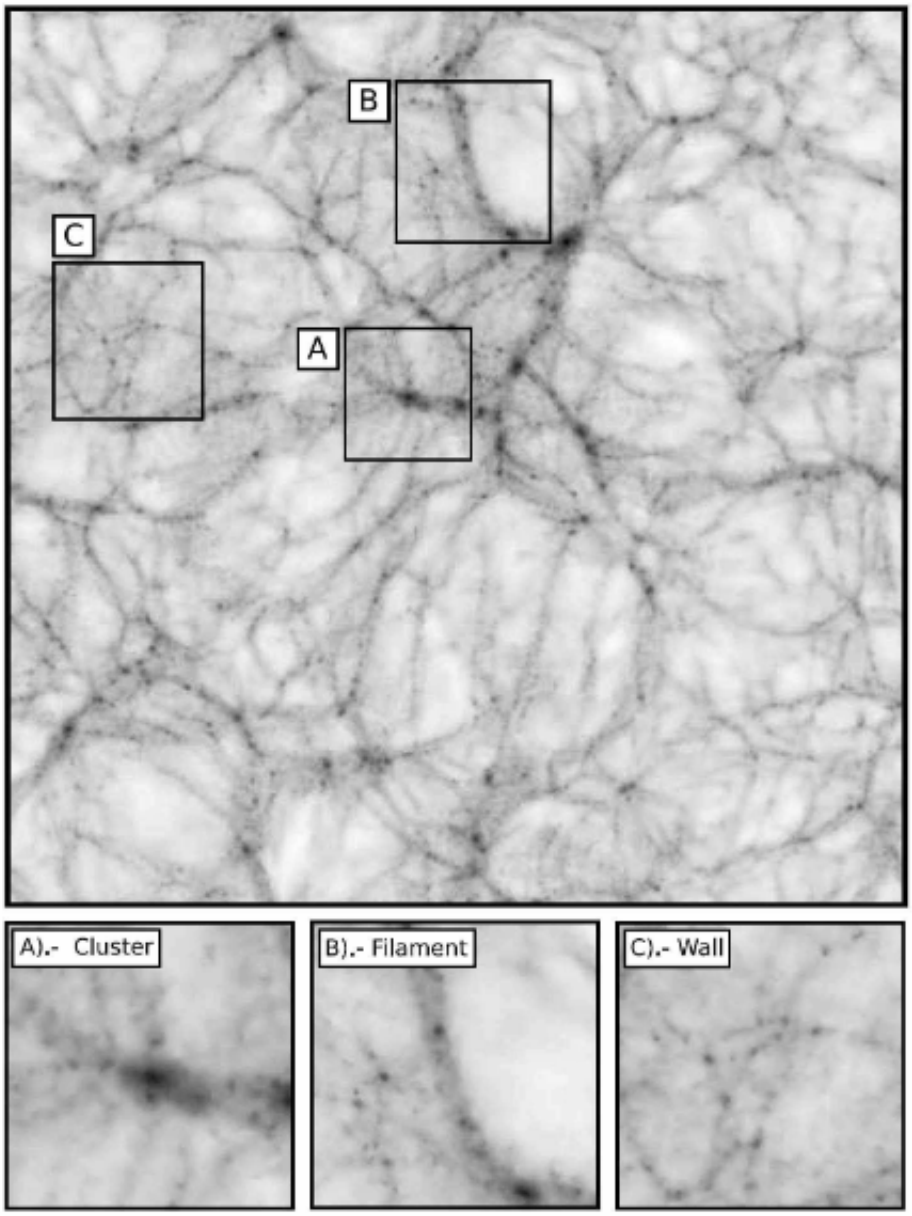


Figure 2: **Structures** In this figure we can see the different kinds of structures we find in the cosmic web. (Aragon Calvo, 2007)

### 1.2.2 Walls

Walls within the Cosmic Web look slightly like filaments, but where the filaments are the highways, the walls are more like the country side roads. Instead of connecting two high-density regions with each other, walls mostly connect voids to filaments and sometime to nodes. They also have a completely different shape compared to the filaments. They look like sheetlike membranes and they surround the void regions, which is exactly why they are called walls.

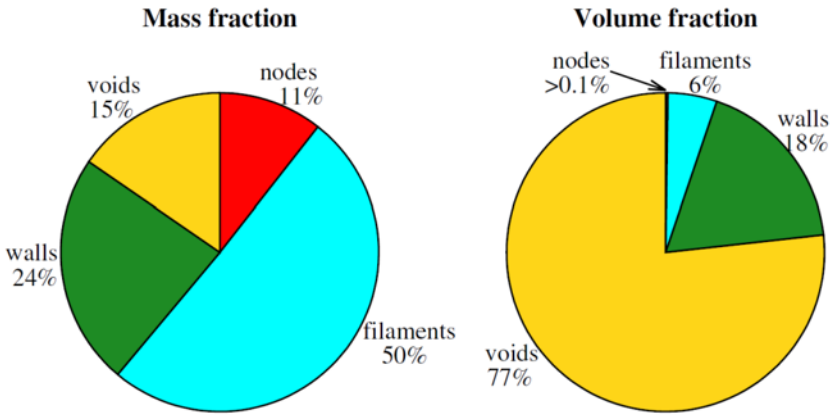


Figure 3: **Mass and Volume fractions** In this figure we find the mass distribution (left) and the volume distribution (right) of the different types of structures in our universe. (Cautun et al., 2014)

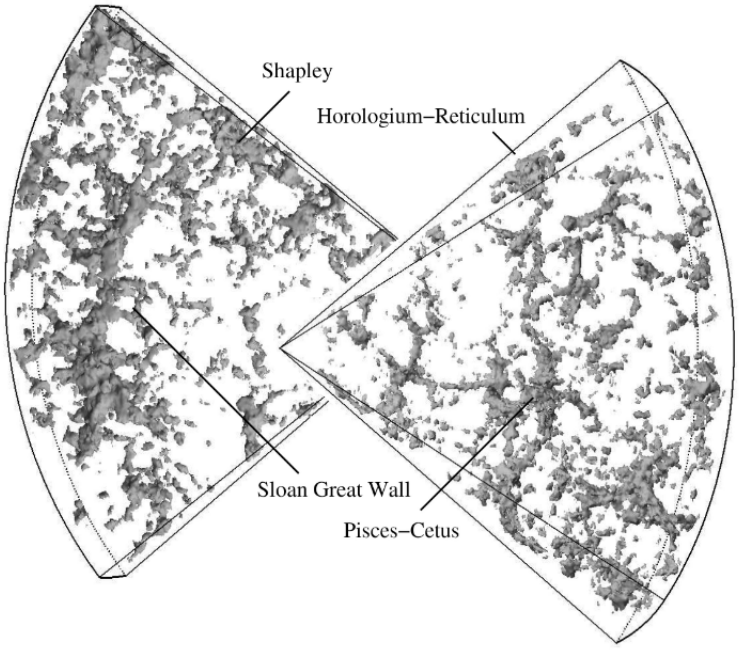


Figure 4: The structure of our local cosmic neighbourhood based on the 2df Redshift survey. We can clearly see the Shapley region and the Sloan Great Wall. (Jones and van de Weygaert, 2014)

These structures are very hard to find. Filaments consist of a lot of very luminous galaxies, which make them very easy to identify, but the walls consist mostly of small galaxy with a low luminosity (Cautun et al., 2014). We also find walls consisting of super clusters. When we look at the spacial structure outlined by these clusters we find flatted structures. These clusters are often referred to as Great Walls. A particular outstanding great wall is the Sloan Great wall (Gott III

et al., 2005), it is one of the largest structures known in our universe. The Sloan Great Wall was discovered with the Sloan Digital Sky Survey. It is also shown in figure 4, which are the smoothed results of the 2df Redshift survey (Jones and van de Weygaert, 2014) (Colless et al., 2001).

### 1.2.3 Nodes

Noes, often associated with cluster or super clusters are the high density regions of the Cosmic Web. Using the gravitational instability theorem we see that structure started from small fluctuations in the primordial density field and velocity perturbations (Peebles, 1980). These structures started to grow when the universe started expanding because of the gravity field around the structures. The higher-density regions started to attract more and more matter, forming even higher densities in bigger structures.

These regions evolved into galaxies, and the galaxies formed gravitational bound regions, called clusters. These clusters formed even bigger structures, called super clusters. As we have seen before, these super clusters are connected to each other by filaments. These filaments are also the primary feeder of matter into the nodes. How this exactly happens in discussed in the next section about cosmic flow (Kraljic et al., 2020). An example of a node in the Bolshoi Simulation (Klypin, Primack and Cantalupo, N.d.) is shown in figure 5.

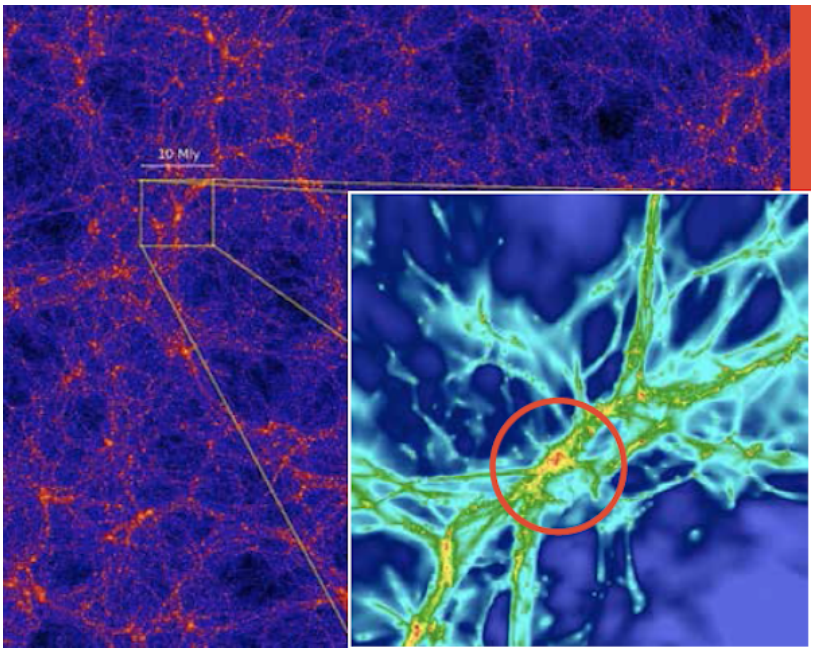


Figure 5: **Node** An example of a node in the Bolshoi simulation (Klypin, Primack and Cantalupo, N.d.).

Looking at the total cosmic web, nodes represent the rare events in the the matter distribution on this scale (Van de Weijgaert and Bond, 2005). As can be seen in figure 3, the volume fraction of the nodes is less than 0.1 percent, which implies that they are very rare. But looking at the mass fraction of the nodes in figure 3, we find that 13 percent of all mass is contained within the nodes, this again illustrates the high-density of the nodes compared to other components of the cosmic web.

Our own galaxy is part of the local group, which is part of the Lanaikea Super Cluster, so the Milky-Way lies within a node.

### 1.2.4 Voids

Voids form a prominent aspect of the Cosmic Web at the megaparsec scales if you look at the volume distribution, but they are significantly less important when looking at the mass fractions. In this way they are exactly opposite from nodes, which is a logical result since the voids are the lowest density regions in our universe (van de Weygaert, 2014).

Voids are enormous regions which are almost empty, of sizes of 20 - 50 $h^{-1}$ (Van De Weygaert and Platen, 2011). In most cases they have a round shape and they are surrounded by sheet-like structures as walls and filaments. If we use a void-based model of the evolution of the matter distribution at cosmological scale we see that voids locate the scale at which density perturbations are decoupled from the Hubble flow (Van De Weygaert and Platen, 2011).

As voids evolve over time they are merging together to form even larger voids, but small voids can also disappear in larger over-dense regions such as walls and filaments (Sheth and van de Weygaert, 2004).

## 1.3 Anisotropy of the Cosmic Web Flow Field

The cosmic web is not a static structure, it evolves over time. In the early stages, there was almost no structure, only on a very small scale, but over time the universe expands and the small scale structure grows into a very complex multi-scale structure. Matter is distributed and redistributed on a continuous base. This raises the questions: which path follows matter in this time evolution and how can we find these patterns? The answer to this question lies in the gravitational instability theorem (Zel'Dovich, 1970), (White and Silk, 1979), (Sheth, Mo and

Tormen, 2001). This theory predicts mass flowing from voids towards nodes along walls and filaments. As can be seen in figure 6 we find that the voids are losing mass over time where the nodes are gaining mass. Most mass from the voids moves to the filaments and walls, from the walls to the filaments, and from the filaments to the nodes. This can also be seen in figure 7 (Cautun et al., 2014).

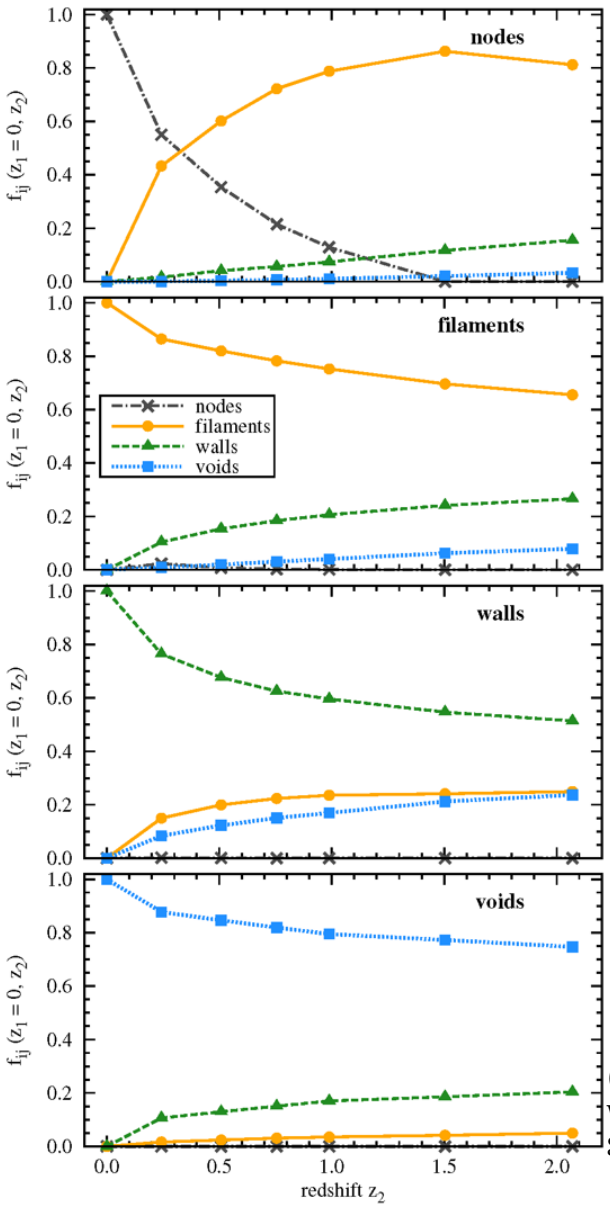


(a) From right to left the density fraction contained in the structure.

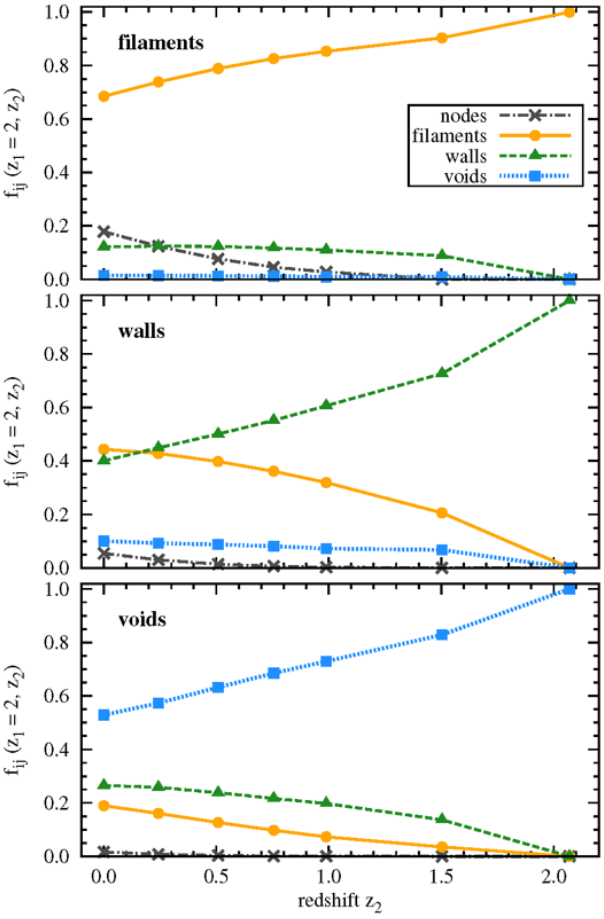


(b) From right to left the density fraction outflow towards the structure. (Romano-Diaz and van de Weygaert, 2007)

Figure 6: **Density** Density changes from z=0 to z=2. (Cautun et al., 2014)

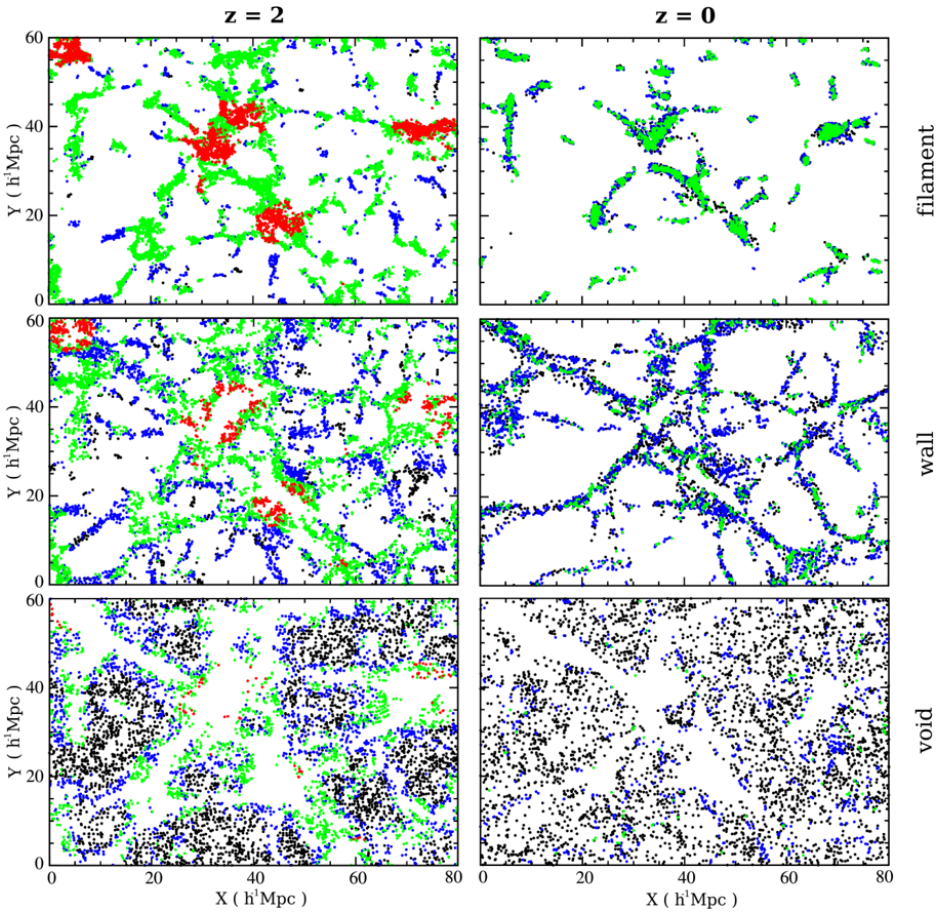


Figure 7: **Density change** Plots indicating the difference between z=2 (right) and z=0 (left). (Cautun et al., 2014)

Any over-dense region, like walls and filaments, are constantly in motion as the result of the competition between the binding force from self-gravity and the pulling force from the high-density regions like nodes. In the event that the self-gravity force is smaller than the gravity force from the high-density regions, which is often the case for walls and filaments, there will be a net movement of particles in the direction of the node. This constant stream of particles is called cosmic flow. The mechanism behind cosmic flow is also the reason for the elongated shape of the walls and filaments.

These cosmic flow patterns are not only found in simulations, but also in our local universe. The IRAS-PSCz catalog contains over 8500 galaxies and can be considered as a good overview of the local cosmic neighbourhood. This data-set was used to determine the velocity field in the local super-cluster, but also in the coma cluster, the sculptor void and the Perseus-Pisces & Cetus wall (Romano-Diaz and van de Weygaert, 2007). The fields are shown in figure 7. If we look at these plots we can clearly see the movement from lower density regions (blue) towards high-density regions (red). We can also see the differences between the different kinds of structures,

like we see a totally different pattern for the coma cluster compared to the Sculptor void.

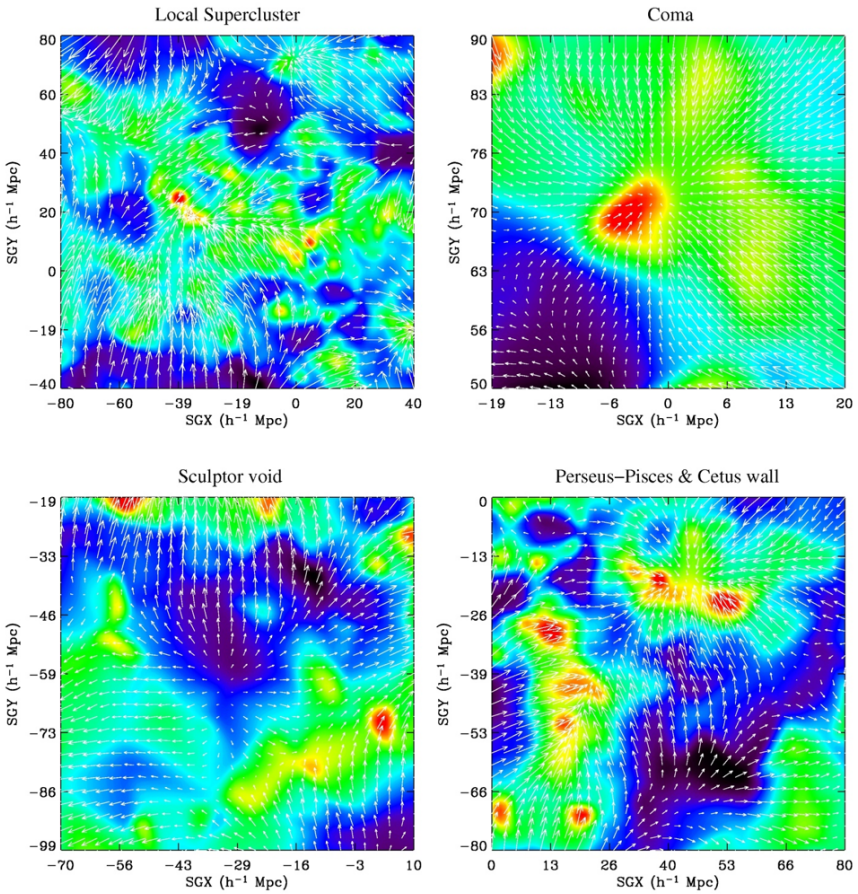


Figure 8: **Flow Streams** Flow streams in our local universe based on the PSCz survey. (Romano-Diaz and van de Weygaert, 2007)

It would be very interesting to expand the maps into a third dimension, in order to approach the real situation. A really good example of such a three-dimensional velocity field is the map of Laniakea, which is our local super cluster interacting with Perseus-Pisces (Tully, Courtois and Sorce, 2016). The plot is shown in figure 9 together with an impression of the velocity field around the Milky-Way.

If we look at this map we see the different colors of the lines in Laniakea and the lines in Perseus-Pisces. In this plot, the black line indicates a negative flow and the red line indicate a positive flow, so we see that matter from the local super cluster is moving towards Perseus-Pisces. This is the reason we call the Perseus-Pisces cluster together with the Coma-cluster the Great Attractor. If we now look at figure 10 we see the complete morphology of the shear velocity field in our local cosmic neighbourhood (Hoffman et al., 2017).

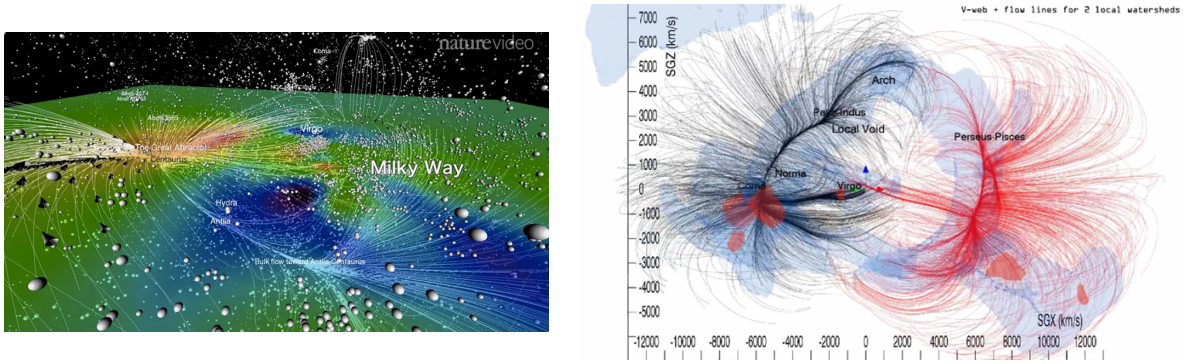


Figure 9: **Models of Laniakea** Impression showing data from the Laniakea super cluster (left) and the flow lines from this cluster(right). left: (Tully et al., 2014), right: (Tully, Courtois and Sorce, 2016)

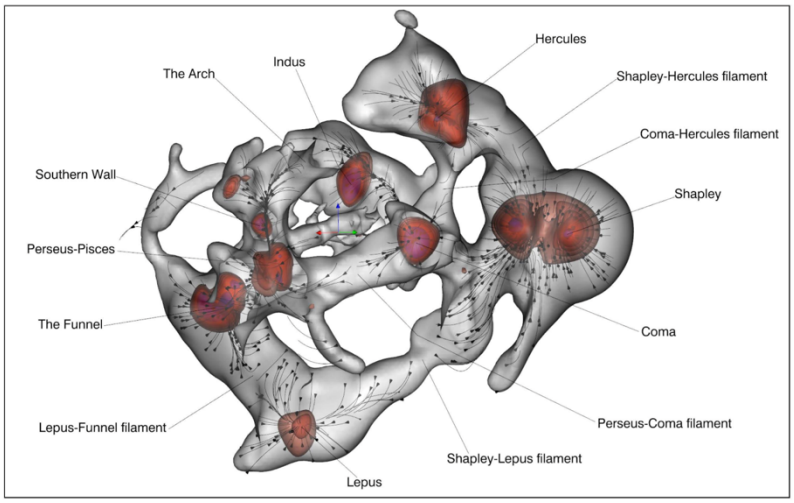


Figure 10: **3D model** A 3D model showing the morphology of the shear velocity in the cosmic web. (Hoffman et al., 2017)

If we look at the most recent research we find the plots shown in figure 11. On the left side we see a density plot with the movement direction of the matter of a region containing a couple of nodes connected by filaments and walls. If we then look on the right side we see the streamlines of the velocity plotted on the density field. If we firstly look at the nodes, we find that the matter is mostly moving towards the nodes and that we find vorticity in these high-density region. We almost not see streamlines moving away from the nodes.

If we then look at the lowest density regions in the plot we see that all streamlines are leaving these regions, moving towards mostly walls and a couple of filaments. This means that matter is leaving the voids via the walls and filaments. From the walls it moves mostly into the bigger filaments, eventually reaching the nodes.

This plot describes exactly the results we want to find in this project. We will not look at a complete field, but we will look at every node to determine the inflow regions and the outflow regions.

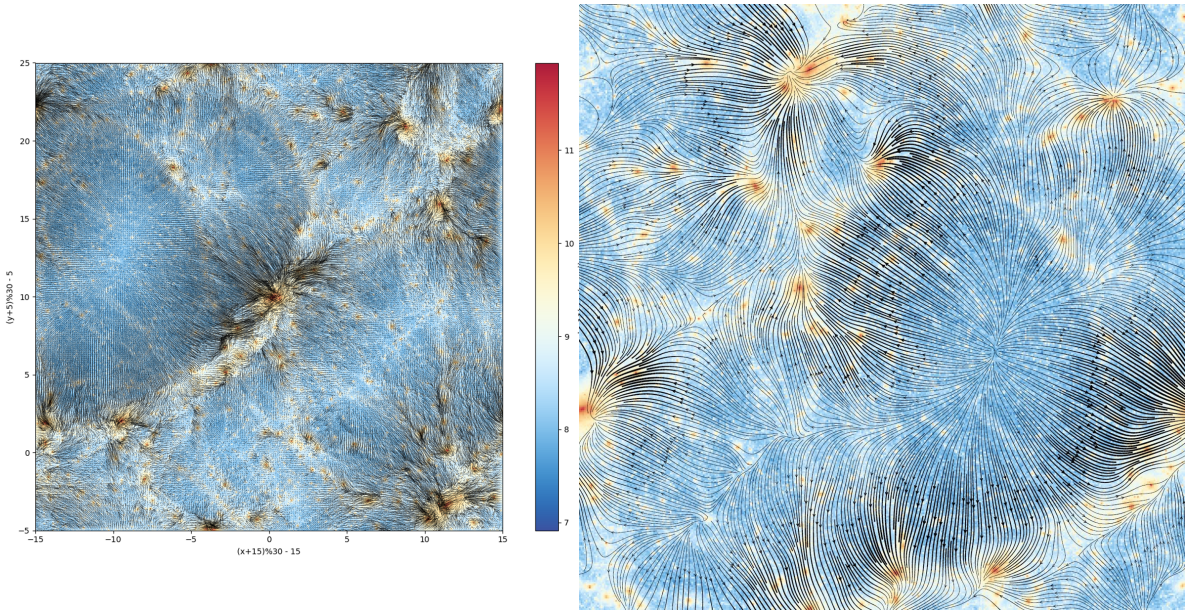


Figure 11: **Flow lines** The field (left) and the field with flow lines (right) (Rieder, de Weijgaert and Portegies-Zwart, 2020)

# 2 Identifying the Cosmic Web

As seen in chapter 1, the universe is not uniform on a megaparsec scale. The matter and galaxy distribution follow a complex inter-connected multi-scale structure. These complex structures are found throughout the entire observable universe at different scales. The structure defines a complicated special pattern, depicting a very rich geometry over multiple shapes and morphology's (Libeskind et al., 2018).

In order to improve the understanding of the Cosmic Web, there is need for a method able to extract topological and morphological information from a data-set. (This could be the data from a survey, or the results of a N-body simulation.) In the end we want to be able to classify the data-points into components of the Cosmic Web (nodes, filaments, and walls). This is a major challenge because of the complex, multi-scale patterns, the large asymmetries and a wide range of densities.

In this project we are using the MMF/NEXUS method (Aragon-Calvo, van de Weygaert, Jones and van der Hulst, 2007) (Cautun, van de Weygaert and Jones, 2013). This method is able to analyse the geometrical properties of the structure as well as taking into account the multi-scale nature of the cosmic web and analyze it.

## 2.1 A short introduction

There have been developed many methods, all working for different kinds of data. There have been developed topological methods, which assess the Cosmic Web structures using the connectivity and topological characteristics of the fields. A good example of such a method is the DisPerSe method, developed by Sousbie (Sousbie, Pichon and Kawahara, 2011). This method identifies topological features, so that they can be used to identify the full set of structural components of the Cosmic Web. Another good example of a topological method is a void identifying formalism. The method is based on the Watershed Transform (Kornilov and Safonov, 2018). This transformation is used to identify under-dense regions such as voids. An implantation of this method can be found in the ZOBOV formalism (Neyrinck, 2008) or in the Watershed Void Finder formalism (Platen, van de Weygaert and Jones, 2008).

In 2010, Aragon-Calvo and others came up with an extension to this method called Spineweb (Aragon-Calvo, Van De Weygaert and Jones, 2010). This method consists of an elaborate scheme to identify various components on a purely topological basis. Spineweb is able to identify these

characteristics around the voids found by applying the Watershed Transform on the density field. The basic version only works on one scale, but the more elaborate version is able to implement a multi-scale version of the algorithm (Aragon-Calvo et al., 2010) (Aragon-Calvo and Szalay, 2013).

Another group of methods are the so-called stochastic methods. These methods are based on geometrical stochastic properties. A very good example of a formalism is the Bisous formalism (Tempel, Stoica, Martinez, Liivamagi, Castellan and Saar, 2014). This method is able to identify galactic filaments on a multi-scale level. It is based pm a Baysian sampling method which is used to select certain geometrical structures, in this case galactic filaments. The Bisous method can be applied to galaxy surveys like the Sloan Digital Sky Survey (SDSS) (Tempel, Tamm, Gramann, Tuvikene, Liivamagi, Suhhonenko, Kipper, Einasto and Saar, 2014).

Another class of methods are the phase-space methods. These methods look at the phase-space properties of evolving mass distributions. They are mostly used when studying the dynamical properties of Cosmic Web formation. The method is based on the concept that the intrinsic velocity dispersion of matter is small in the very early universe. We can see this as the evolving spacial mass distribution appearing to be a three-dimensional sheet folding itself into a six-dimensional phase-space. A good example of this method are described by Abel et al. (Abel, Hahn and Kaehler, 2012).

We have seen a lot of methods by now, however a large part of the methods fall into a different category, namely the Geometric-Hessian based methods. These methods use the Hessian matrix of the density, tidal, or velocity fields, in order to extract geometrical and morphological information. An example of this method is the tidal classification method by Hahn et al. (Hahn et al., 2007). This method is based on local-stability criteria for orbits of particles much like the Zel'dovich approximation (Zel'Dovich, 1970) (White, 2014).

## 2.2 MMF/NEXUS method

The method we base our work on is MMF/NEXUS. MMF stand for Morphology Filter Formalism and this method was developed by Aragon-Calvo in 2007 (Aragon-Calvo, van de Weygaert, Jones and van der Hulst, 2007). The MMF/NEXUS method uses the Scale-Space point of view to look at structure. It takes the multi-scale nature of the Cosmic Web into account by assessing each point at different scales based on the Hessian of the field. It also has fully adaptive framework for the classification of data based on local field, rather than only taking the global field into account.

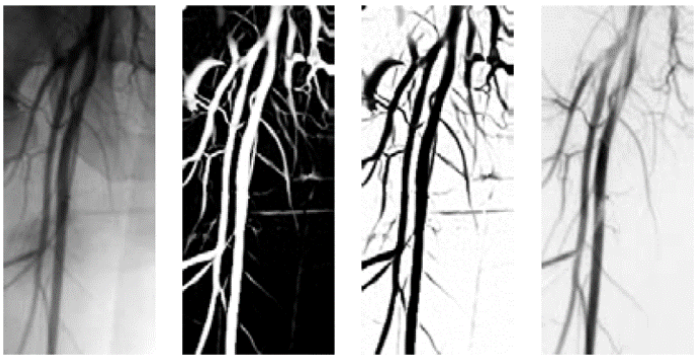

Figure 12: **Blood vessels** Blood vessels at different scales identified using a similar algorithm as NEXUS. (Frangi et al., 1998)

At the same time, some morphological filters are used to classify each point as node, filament, or wall. This results in a complete data-set with each data-point classified in one of the three categories. This Space-Scale point of view is not new, it has previously been used in the medical field, there an algorithm based on this principle was developed to identify a web of blood vessels (Frangi et al., 1998). As we can see in figure 12 the blood vessels form a multi-scale structure very similar to the cosmic web structures as can be seen in figure 13.

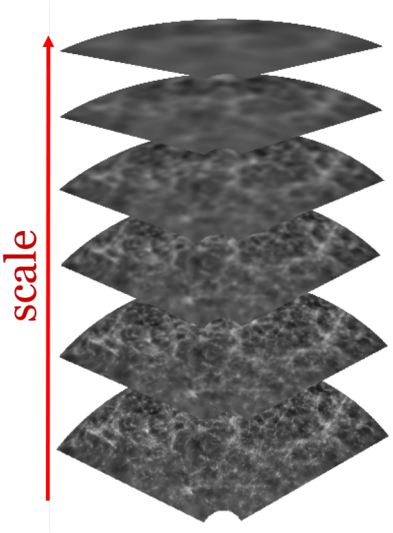


Figure 13: **Scales** As seen in this figure, the smaller the scale, the more details are visible. (Aragon Calvo, 2007)

Although we can clearly see parallels between the two applications, the algorithm had to be heavily altered to make it useful for cosmic applications. The NEXUS algorithm has an unique approach to the multi-scale structure, where most Hessian-based methods are defined on one particular smoothing scale, the NEXUS algorithm runs on multiple scales and selects the classification of the most appropriate scale, which is determined for every point. The normal version of

NEXUS uses a Gaussian smoothing filter at a lot of different scales, where the NEXUS+ formalism uses a logarithmic Gaussian version. The difference between the two versions is very well shown in figure 14.

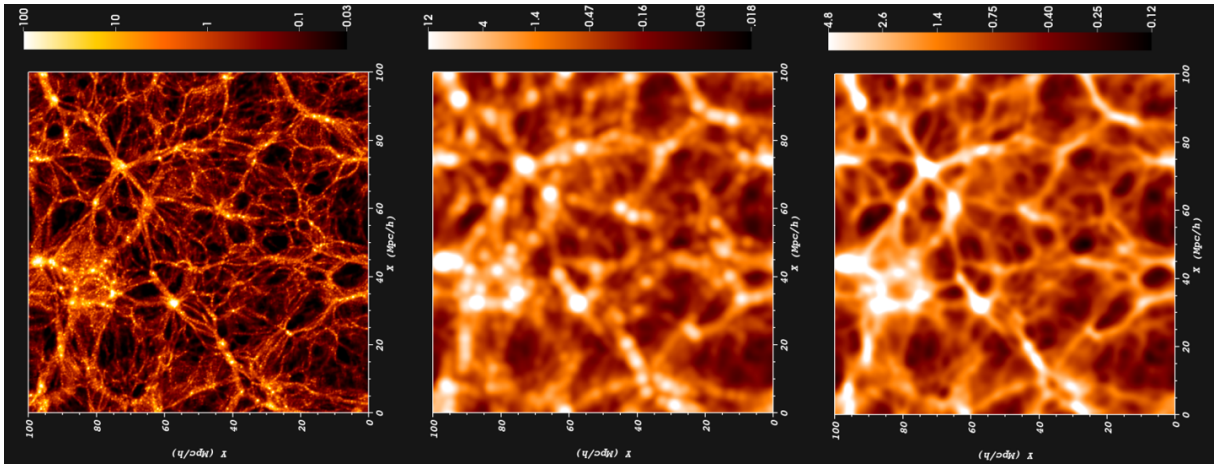

Figure 14: **Difference NEXUS/NEXUS+** In this figure we can see the difference between a Gaussian filter (middle) and a log-Gaussian filter (right) compared to the input (left). (Cautun, van de Weygaert and Jones, 2013)

The final outcome of the MMF/NEXUS formalism is a data-set, with every point sorted into one of the components. The method under went a long evolution. The first version was published in 2007 by Aragon-Calvo and others (Aragon-Calvo, van de Weygaert, Jones and van der Hulst, 2007) as described earlier and the first results were published (Aragon-Calvo, Jones, van de Weygaert and van der Hulst, 2007). In 2010, the first two long articles were published using this method. Aragon-Calvo and others did the first systematic study of the Cosmic Web using MMF/NEXUS (Aragon-Calvo, Van De Weygaert and Jones, 2010) and a study by Jones and others discussing the galaxy alignments in the Cosmic Web based in the SDSS (Jones, Van De Weygaert and Aragon-Calvo, 2010).

In 2013 the method was greatly improved and expanded (Cautun, van de Weygaert and Jones, 2013). In 2014, the first studies using the improved method were published (Cautun et al., 2014). A more recent study using the MMF/NEXUS formalism is done by Ganeshaiah Veena and other about spin and shape alignments of halos in the Cosmic Web (Ganeshaiaha Veena et al., 2018). But MMF/NEXUS is not just one single algorithm, there are a lot of different flavours, all working on the basis of different fields determined by physical characteristic. Some examples of these fields are the density field, the shear velocity field, the shear tidal field and the gravity field. In this project we use a version of MMF/NEXUS based on the density field.

## 2.3 A general description of NEXUS+

The NEXUS and NEXUS+ algorithms are used to find, point-, line- and sheetlike structures in the input field. In the case of the Cosmic Web, these structures will be the nodes, filaments, and walls found in the input field. The NEXUS+ algorithm uses the following steps to identify the components (Cautun, van de Weygaert and Jones, 2013):

1. Apply a Log-Gaussian filter to the field of width $R_n$
2. Compute the Hessian Matrix eigenvalues of the smooth field
3. Assign each point to a cluster, filament or wall component based on the eigenvalues
4. Repeat step 1 to 3 over a range of values for $R_n$ in order to get a range of scales
5. Combining all values found on each scale and obtain scale-independent structure categorization.
6. Using physical criteria to determine the detection threshold

A more elaborate description of each step is given below.

### 2.3.1 Step 1: Log-Gaussian filter

Suppose we have a field f, and now we want to filter the field with a logarithmic Gaussian filter with a width of $R_n$. We first have to introduce a new variable g which is defined as the logarithm of f as seen in equation 1.

$$g = \log_{10} f \tag{1}$$

and we will introduce the smoothed field on scale $R_n$ as:

$$g_{R_n}(\vec{x}) = \int d^3y g(\vec{y}) W_{G,R_n}(\vec{x}, \vec{y}) \tag{2}$$

with $W_{G,R_n}$ the Gaussian filter of width $R_n$.

Using these equations we find that there are three steps needed to filter the field with a logarithmic Gaussian filter, namely:

1. Use equation 1 to calculate the logarithm of the original field.
2. Apply the Gaussian filter of width $R_n$ to the field.

3. Find the smoothed field of $f$ by taking the exponential of $g$.

In order to make the calculations slightly simpler the Gaussian filter in applied in Fourier Space. In practice, this means that:

$$g_{R_n}(\vec{x}) = \int \frac{d^3k}{(2\pi)^3} e^{-k^2 R_n^2/2} \hat{g}(\vec{k}) e^{i\vec{k}\cdot\vec{x}} \tag{3}$$

After this step we want to go back to the field $f$, and have it smoothed. This is obtained by taking the exponential of the field $g$ after the Gaussian filter:

$$f_{R_n}(\vec{x}) = C_{R_n} 10^{g_{R_n}} \tag{4}$$

In this equation $C_{R_n}$ is the multiplication factor needed to assure that the average of the field stays constant under the calculations.

### 2.3.2 Step 2: Eigenvalues

The second step of the algorithm is the calculation of the eigenvalues of the Hessian. For the smoothed field the Hessian is defined as:

$$H_{ij,R_n} = R_n^2 \frac{\partial^2 f_{R_n}(\vec{x})}{\partial x_i \partial y_j} \tag{5}$$

In Fourier Space this can be written as:

$$\hat{H}_{ij,R_n}(\vec{k}) = -k_i k_j R_n^2 \hat{f}_{R_n}(\vec{k}) \tag{6}$$

The eigenvalues of the Hessian are now given by:

$$\det(H_{R_n}(\vec{x}) - \lambda_{a,R_n}(\vec{x})) = 0 \tag{7}$$

with eigenvalues: $\lambda_1 \leq \lambda_2 \leq \lambda_3$.

### 2.3.3 Step 3: Assignment

Using these eigenvalues of the Hessian, we can assign every point to a specific characteristic, namely cluster/node, filament, or wall. This is done using the constraints written in table 1. The first step is to determine the category using the soft constraints. This can be done quantitatively

| Structure | Soft Constraints | Hard constraints |
|---|---|---|
| Cluster/node | $\lvert\lambda_1\rvert \approx \lvert\lambda_2\rvert \approx \lvert\lambda_3\rvert$ | $\lambda_1 < 0; \lambda_2 < 0; \lambda_3 < 0$ |
| Filament | $\lvert\lambda_1\rvert \approx \lvert\lambda_2\rvert \gg \lvert\lambda_3\rvert$ | $\lambda_1 < 0; \lambda_2 < 0$ |
| Wall | $\lvert\lambda_1\rvert \gg \lvert\lambda_2\rvert; \lvert\lambda_1\rvert \gg \lvert\lambda_3\rvert$ | $\lambda_1 < 0$ |

Table 1: Constraints to assign each point to a characteristic using the eigenvalues of the Hessian given in equation 7

using equation 8 where we define $I$ to be a relative strength in each category.

$$I = \begin{cases} \left|\frac{\lambda_3}{\lambda_1}\right| & \text{Cluster/Node} \\ \left|\frac{\lambda_2}{\lambda_1}\right| \Theta\left(1 - \left|\frac{\lambda_3}{\lambda_1}\right|\right) & \text{Filament} \\ \Theta\left(1 - \left|\frac{\lambda_2}{\lambda_1}\right|\right)\Theta\left(1 - \left|\frac{\lambda_3}{\lambda_1}\right|\right) & \text{Wall} \end{cases} \tag{8}$$

We define:

$$\Theta(x) = x\theta(x) \tag{9}$$

In which we define:

$$\theta(x) = \begin{cases} 1 & \text{if } x \geq 0 \\ 0 & \text{otherwise} \end{cases} \tag{10}$$

which is also known as the step-function.

The strength $I$ has a large value in the case that the structural constraints are largely validated where the value is small if the constraints are not satisfied. We can introduce a similar scheme for the hard conditions and multiplying the schemes, results in an accurate distribution of each point with respect to the components. The so called structure signature is defined as:

$$S = I \times \begin{cases} |\lambda_3|\theta(-\lambda_1)\theta(-\lambda_2)\theta(-\lambda_3) & \text{Cluster/Node} \\ |\lambda_2|\theta(-\lambda_1)\theta(-\lambda_2) & \text{Filament} \\ |\lambda_1|\theta(-\lambda_1) & \text{Wall} \end{cases} \tag{11}$$

Where $\theta(-\lambda_a)$ incorporates the conditions in the third column of table 1. In figure 15 we see the different types of structures identified using the algorithm.

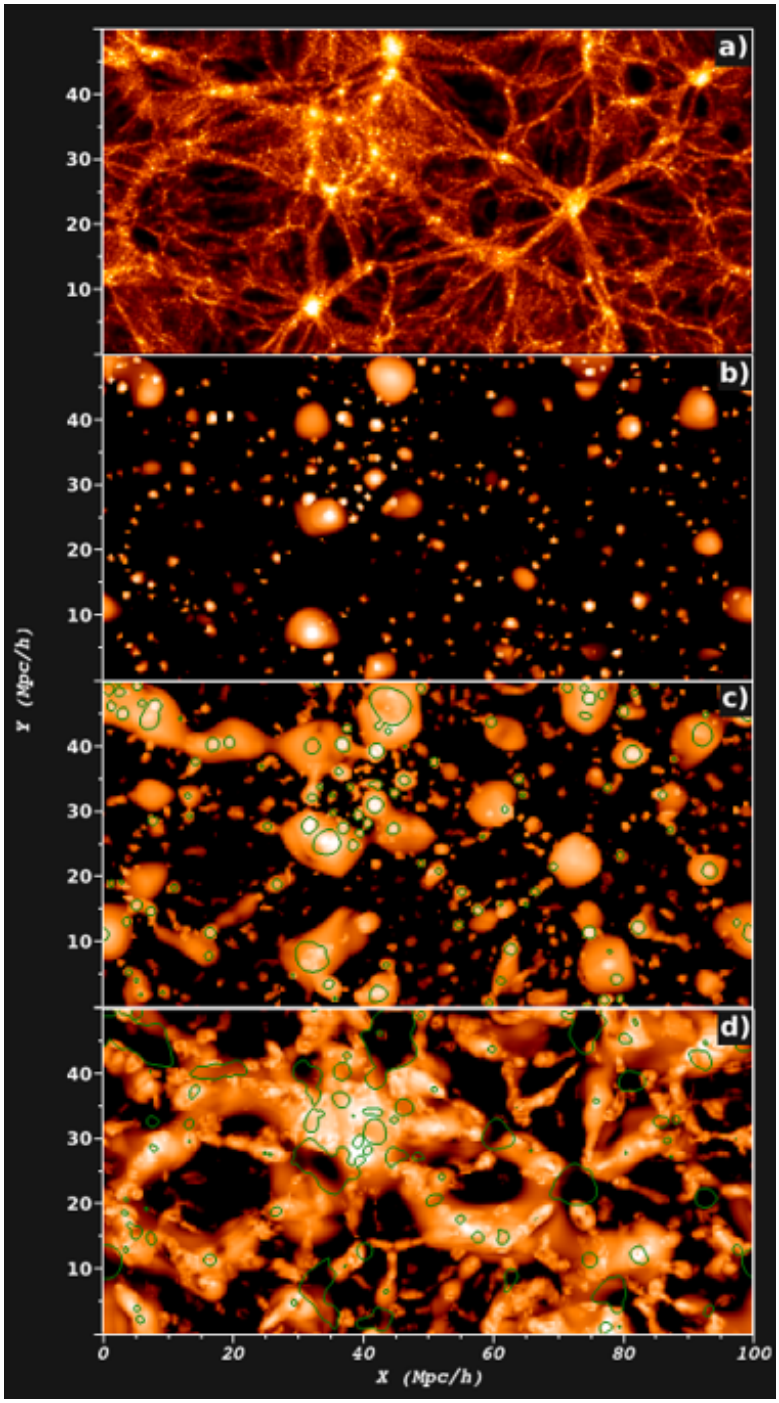


Figure 15: **Results of NEXUS** The different structures as identified by the algorithm. a) density field, b) node, c) filament, d) wall (Cautun, van de Weygaert and Jones, 2013)

### 2.3.4 Step 4: A range of scales

In order to define the cosmic web over a range of structure scales, we have to repeat all of the previous described steps for all scales. The smallest scale must be the scale at which the smallest structures you want to define are found. It turns out that this is often the grid spacing of your

input field. The hierarchy of the smoothing scales is taken to be:

$$R_n = (\sqrt{2})^n R_0 \tag{12}$$

In which $R_0$ is the smallest structure scale. It is found that taking even smaller scales will not result in significant changes (Sato et al., 1998). It is found that in order to detect the most prominent features of the cosmic web we have to choose a value for $R_0$ in the range 0.5 $h^{-1}$ Mpc to 4 $h^{-1}$ Mpc (Cautun, van de Weygaert and Jones, 2013).

This step results in the results of the signature function given in equation 11 for each of the chosen scales for each point on the grid.

### 2.3.5 Step 5: Combination

In order to get a scale-independent map of all characteristics we have to combine them in some way where the strongest signature values are kept over a multi-scale combination. This map will characterize for each point $\vec{x}$ if it is part of a cluster/node, filament or wall.

A structure of a given size will have the largest signature at the same smoothing scale as the size of the structure. This means that we have to define the overall signature at a certain point as the maximum signature at that point over all scales, as seen in equation 13.

$$S(\vec{x}) = \max S_{R_n}(\vec{x}) \tag{13}$$

A comparison between the original input field and the field created using the data from the NEXUS algorithm is shown in figure 16.

### 2.3.6 Step 6: The Detection Threshold

The signature is the result of all detection's in the field. This means that only part of the signature is really structure, and the other parts are noise. In order to filter out the noise, the last part of the algorithm involves the use of physical criteria to find a threshold to identify the valid structures and get rid of the invalid detection's. This means that all values larger than the threshold value correspond to a real structure and all values lower than the threshold are noise. The threshold value for clusters/nodes is found by setting the condition that the structures should be virialized, where the threshold for filaments and walls is determined by the dependence of the mass on the environmental mass.

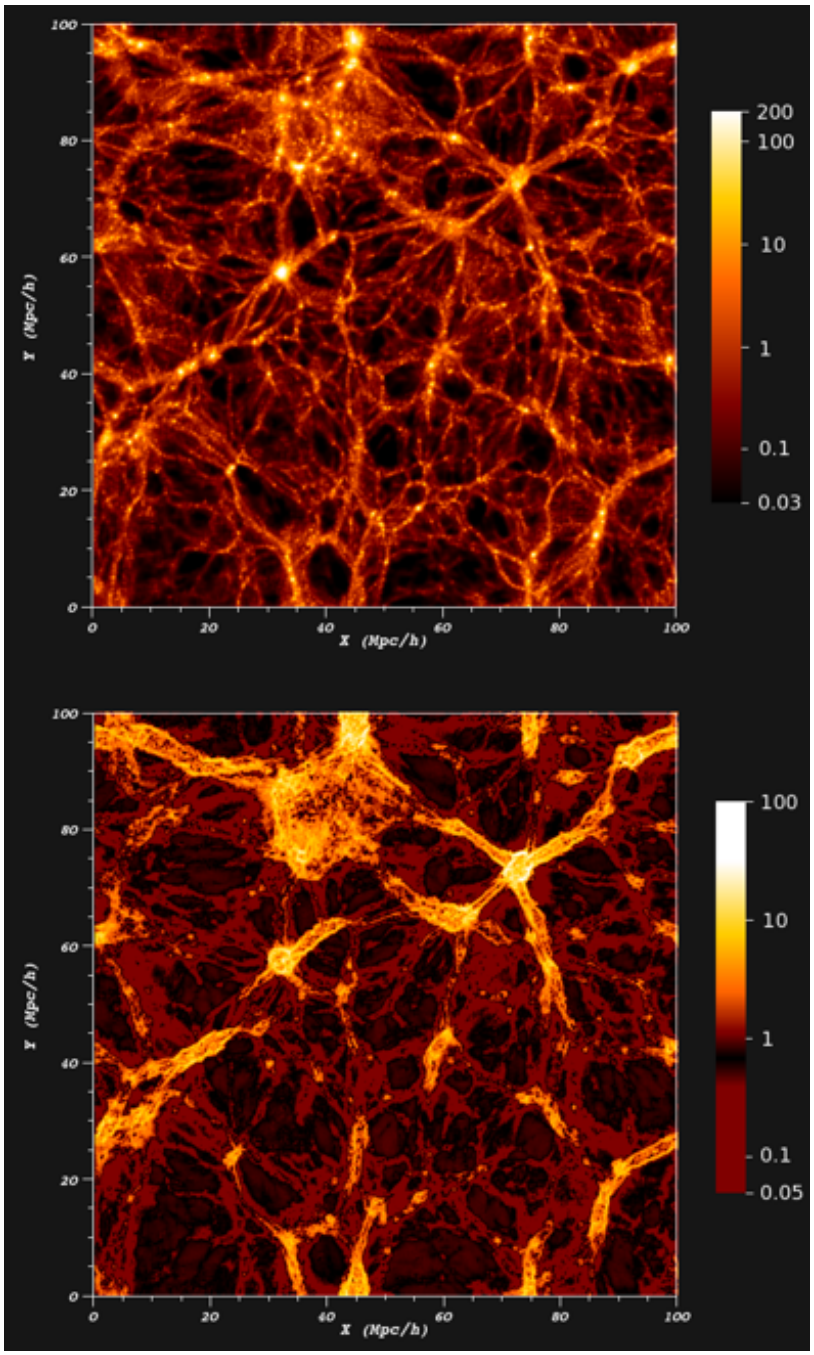


Figure 16: **Comparison input and output** A comparison between the input field (up) and the field created using the NEXUS algorithm (down). (Cautun, van de Weygaert and Jones, 2013)

In order to overcome the cross-contamination, meaning that for example, we identify a certain point to be a filament and a wall at the same time, we set the condition that when a point is previously identified a being part of as a cluster it cannot be identified as a filament, and when a point is identified as a filament it cannot be identified as a wall. So we first identify all points which are clusters, then the filaments and lastly the walls.

# 3 Anisotropy of Cosmic Web flow field

## 3.1 Skyview

The goal eventually is to find the inflow along the filaments towards the nodes and classify it for all nodes to determine the flow direction for the nodes. We do that by looking at sky plots of the surface density projected on the sky, and we will do this following the method of (Rieder et al., 2013). The sky plots will be similar to the ones shown in figure 17.

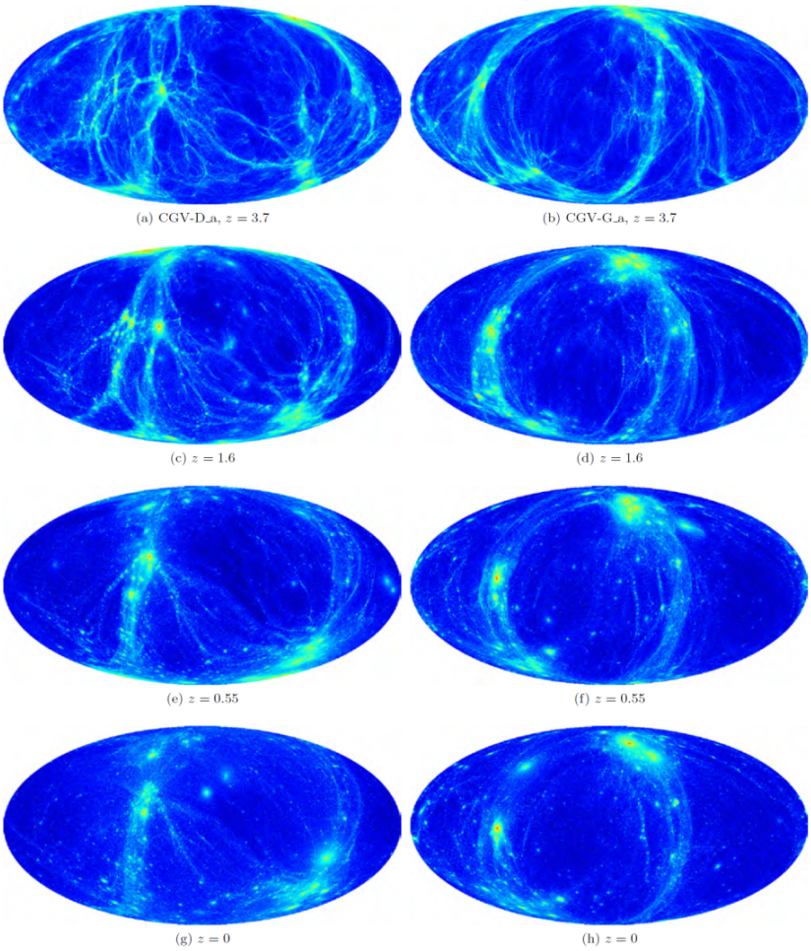


Figure 17: **Mollweide plot of CVG** Mollweide sky projection matter distribution around CGV halos. (Rieder et al., 2013)

We will be specifically interested in the anisotropy of the plots and we would like to be able to classify it. This is not a new problem. In 1986 Villumsen and Davis found the velocity fields as shown in figure 18 around some nodes and tried to classify them. They came up with the idea to use spherical harmonics to identify the patterns and this is exactly what we are going to do (Villumsen and Davis, 1986).

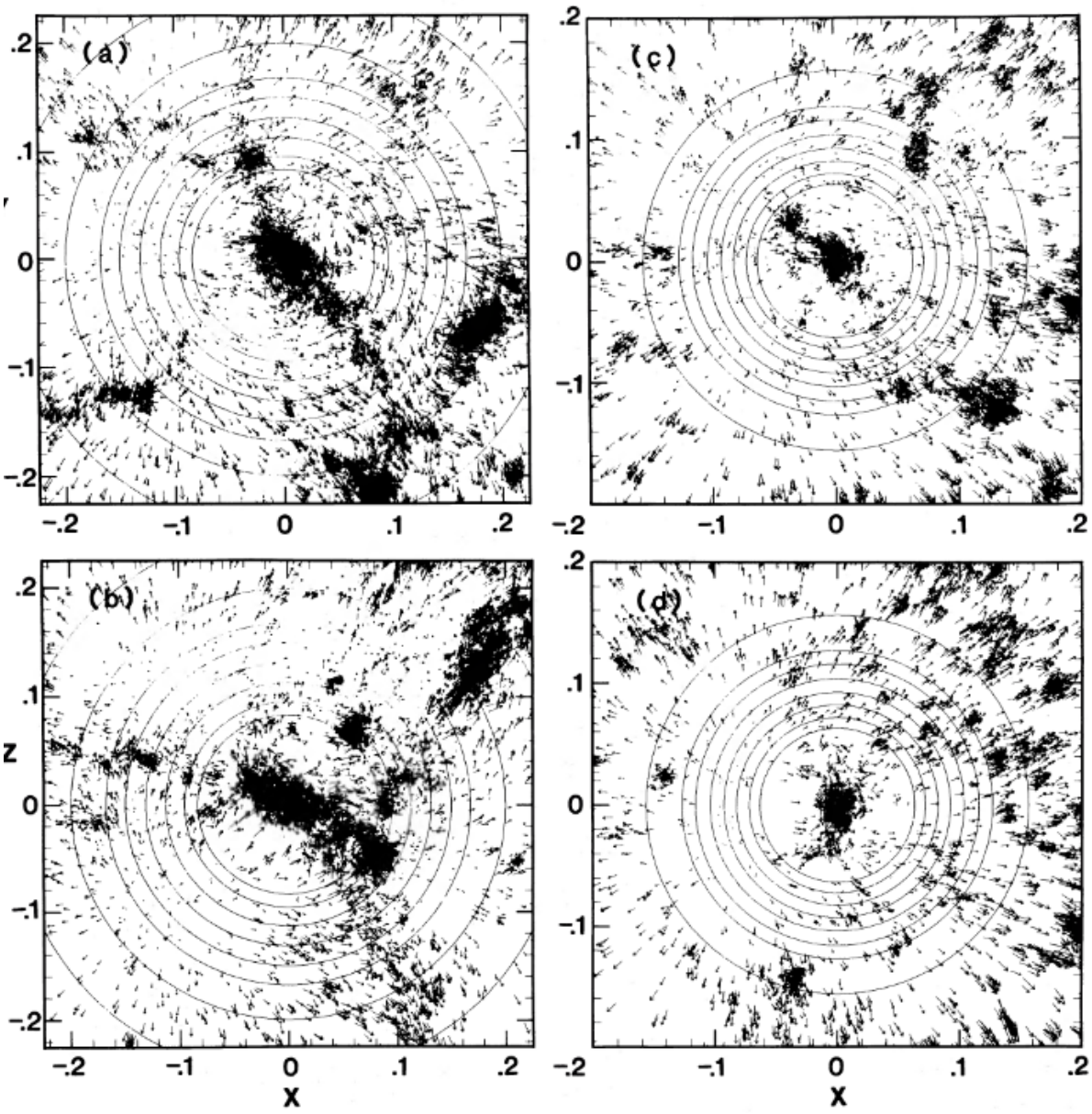


Figure 18: **Velocity field around clusters** Plots showing the velocity fields (indicated by arrows) and the particle distribution around some nodes. (Villumsen and Davis, 1986)

## 3.2 Spherical Harmonics

Spherical harmonics are most often introduced in the field of quantum physics, where they cover the angular dependence of the Laplacian operator. This angular dependence is given by:

$$\frac{\Phi(\phi)}{\sin\theta}\frac{d}{d\theta}\left(\sin\theta\frac{d\Theta}{d\theta}\right)+\frac{\Theta(\theta)}{\sin^2\theta}\frac{d^2\Phi(\phi)}{d\phi^2}+n(n+1)\Theta(\theta)\Phi(\phi)=0 \tag{14}$$

### 3.2.1 The azimuthal dependence

If we separate equation 14 into variable we find that the azimuthal dependence, that is the dependence on $\phi$, looks like the following equation:

$$\frac{1}{\Phi(\phi)}\frac{d^2\Phi(\phi)}{d\phi^2} = -m^2 \tag{15}$$

This equation can be solved and we find the following exponential solutions:

$$\Phi(\phi) = \begin{cases} e^{im\phi} \\ e^{-im\phi} \end{cases} \tag{16}$$

We can check if these conditions satisfy the orthogonality condition:

$$\int_0^{2\pi} e^{im_1\phi}e^{-im_2\phi}d\phi = 2\pi\delta_{m_1m_2} \tag{17}$$

So the orthogonality condition is indeed satisfied. We can also use equation 17 to calculate the normalization constant, and by allowing $m$ to be positive or negative we find the following solution:

$$\Phi_m = \frac{1}{\sqrt{2\pi}}e^{im\phi} \tag{18}$$

### 3.2.2 The polar dependence

In order to find the polar dependence, so the $\theta$ dependence we need to rewrite equation 14 slightly. We can use equation 18 to obtain the following equation:

$$\frac{d^2\Phi(\phi)}{d\phi^2} = -m^2\frac{1}{\sqrt{2\pi}}e^{im\phi} = -m^2\Phi(\phi) \tag{19}$$

Using this equation we can find the $\theta$ dependence of equation 14. This results in:

$$\frac{1}{\sin\theta}\frac{d}{d\theta}\left(\sin\theta\,\frac{d\Theta(\theta)}{d\theta}\right) + \left[n(n+1) - \frac{m^2}{\sin\theta}\right]\Theta(\theta) = 0 \tag{20}$$

This equation is equivalent to the associated Legendre equation which is given by:

$$\frac{1}{\sin\theta}\frac{d}{d\theta}\left(\sin\theta\,\frac{dv}{d\theta}\right)+\left[n(n+1)-\frac{m^2}{\sin\theta}\right]v=0 \tag{21}$$

The solution of this equation is the associated Legendre functions of $\cos\theta$ which gives $\Theta(\theta) = P_n^m(\cos\theta)$. To include the negative values of $m$ we use Rodrigue's formula and we will end up with the following definition for the polar dependence:

$$P_n^m(\cos\theta)=\frac{1}{2^n n!}(1-x^2)^{m/2}\frac{d^{m+n}}{dx^{m+n}}(x^2-1)^n,\ -n\le m\le n \tag{22}$$

Using the relations between this formula for positive and negative $m$ and normalizing the equation 22 we obtain the following solution for the polar dependence:

$$\Theta_n^m=\sqrt{\frac{2n+1}{2}\frac{(n-m)!}{n+m)!}}P_n^m(\cos\theta) \tag{23}$$

### 3.2.3 Spherical Harmonics Equation

In order to describe the complete angular dependence of the solutions of the Laplacian equations we need to combine the azimuthal and the polar dependence. Using the orthonormal equation given in equation 18 and equation 23 we find the following solution(Arfken and Weber, 2005):

$$Y_n^m(\theta,\phi)\equiv(-1)^m\sqrt{\frac{2n+1}{2}\frac{(n-m)!}{n+m)!}}P_n^m(\cos\theta)e^{im\phi} \tag{24}$$

The factor $(-1)^m$ is not needed, but it is allowed to add the term because equation 15 is linear and homogeneous. The factor is added in most literature because it will result in alternating solutions and this makes a lot of calculations easier. The first few spherical harmonics are shown in figure 19.

## 3.3 Laplace Series

In a similar way as to how we can use the Fourier Series to write a formula as a series of infinitely many terms in as many dimensions as you need we can use spherical harmonics to write a function as a sum of terms when it is defined on the surface of a sphere. This is called the Laplace series and is defined by:

$$f(\theta,\phi)=\sum_{m,n}a_{mn}Y_n^m(\theta,\phi) \tag{25}$$

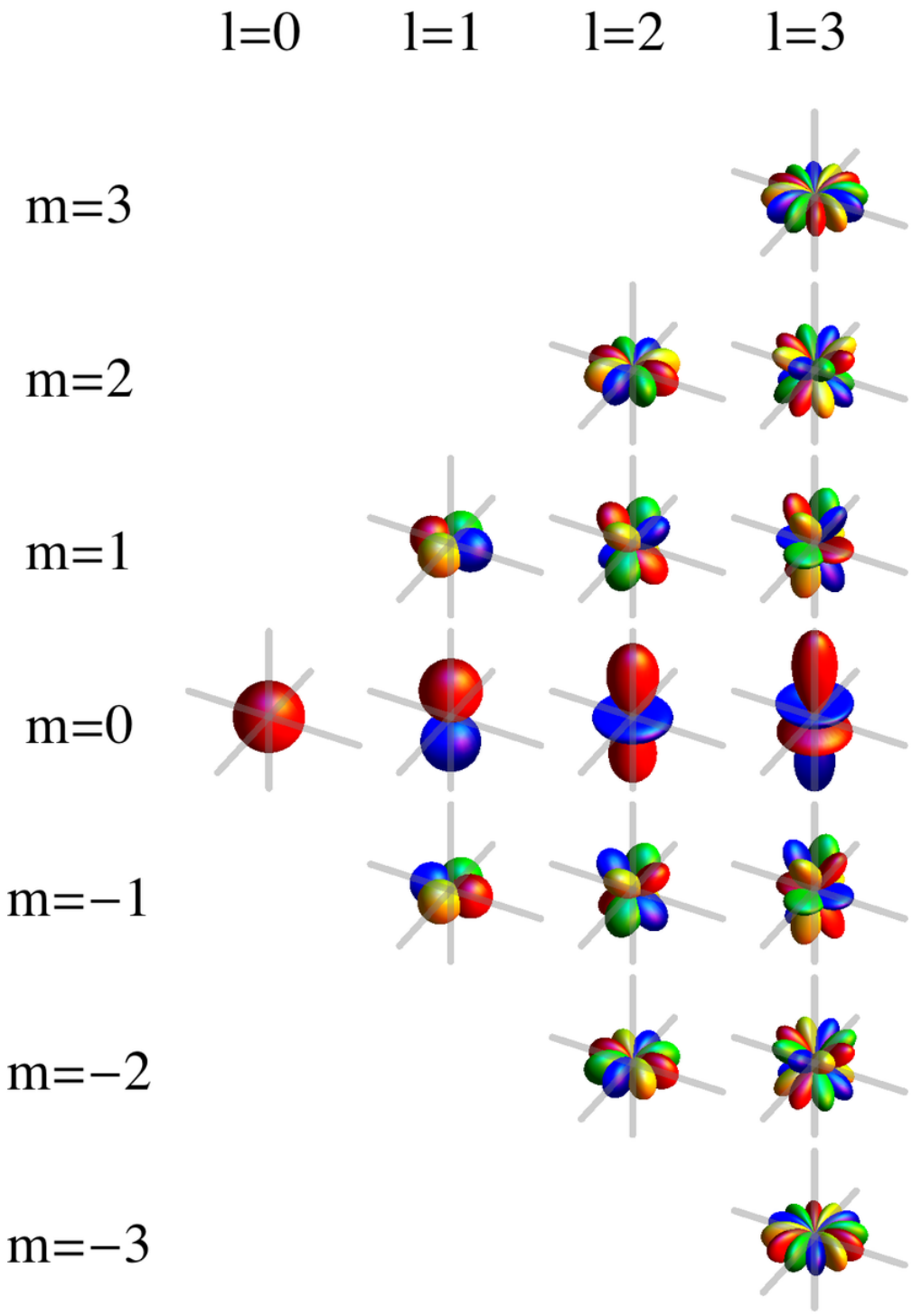


Figure 19: **Spherical Harmonics** Plots of the solutions of the first spherical harmonics(*Spherical Harmonics*, N.d.)

### 3.3.1 Inverse Spherical Harmonics

In order to find the value of $a_{mn}$ or in later stages even $C_l$ we need to define an inverse form. This can be done taking the complex conjugate of equation 24. Taking the complex conjugate can be done by setting $m = -m$ in the original equation. This does result in a problem with the Legendre polynomial (Harber, 2012).

The differential equation for the associated Legendre polynomials is dependent on $m^2$, which implies that the equation is not sensitive to the sign of $m$. As a result, we find that $P_n^m(x)$ must be equivalent to $P_n^{-m}(x)$, which means that the following equation must hold:

$$P_n^{-m}(\cos\theta) = (-1)^m \frac{(n-m)!}{(n+m)!} P_n^m(\cos\theta) \tag{26}$$

rearranging the terms results in the following equivalence relation:

$$P_n^m = (-1)^m \frac{(n+m)!}{(n-m)!} P_n^{-m}(\cos\theta) \tag{27}$$

If we use this relation we can write the complex conjugate as:

$$Y_n^{m*} = (-1)^m \frac{(n+m)!}{(n-m)!} Y_n^{-m} = \sqrt{\frac{2n+1}{2} \frac{(n+m)!}{(n-m)!}} P_n^{-m}(\cos\theta) e^{-im\phi} \tag{28}$$

We can write equation 25 in a continuous form, which results in:

$$f(\theta,\phi) = \int_0^\infty \int_{-n}^{n} a_{nm} Y_n^m dm dn \tag{29}$$

If we multiply both sides by the complex conjugate given in equation 28 we obtain:

$$f(\theta,\phi) Y_n^{m*} = \int_0^\infty \int_{-n}^{n} a_{nm} Y_n^m Y_n^{m*} dm dn \tag{30}$$

As a result of the orthonormal characteristics of $Y_n^m$ we find:

$$f(\theta,\phi) Y_n^{m*} = \int_0^\infty \int_{-n}^{n} a_{nm} dm dn \tag{31}$$

If we now define the equation at a specific point $(m, n)$ and integrate over the solid angle we find:

$$\int_0^{2\pi} \int_0^{\pi} f(\theta,\phi) Y_n^{m*}(\theta,\phi) d\Omega = a_{mn} \tag{32}$$

Which can be written in a discrete form as:

$$a_{mn} = \sum_{\phi=0}^{2\pi} \sum_{\theta=0}^{\pi} f(\theta, \phi) Y_n^{m*}(\theta, \phi) \sin\theta \tag{33}$$

### 3.3.2 Power Spectrum coefficients

In order to find some quantitative results from the spherical harmonics analysis we can look at the power spectrum. For every value of $n$ we can calculate the sum of all spherical harmonics coefficients for the different values of $m$ contained within $n$. Using a generalization of Parseval's Theorem (Arfken and Weber, 2005) we find:

$$C_l(l) = \frac{1}{2l+1} \sum_{m=-l}^{l} |a_{lm}|^2 \tag{34}$$

To be consistent with notation we can define $l = n$.

# 4 Methods and Formalism

In this section, we will discuss some of the methods used in the code.

## 4.1 Coordinate conversion

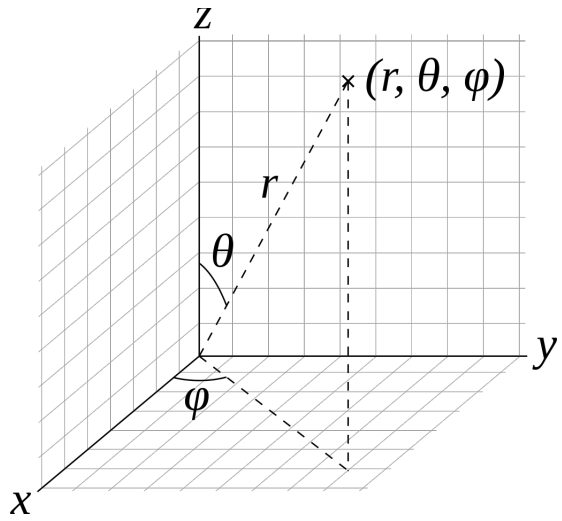


Figure 20: The definition of the spherical coordinates

The conversion between Cartesian coordinates and spherical coordinates can be written as:

$$r = \sqrt{x^2 + y^2 + z^2} \tag{35}$$

$$\theta = \arccos \frac{z}{\sqrt{x^2 + y^2 + z^2}} \tag{36}$$

$$\phi = \arctan \frac{y}{x} \tag{37}$$

All spherical coordinates $(r, \theta, \phi)$ are defined in figure 20. We can also define the coordinate transformation in vector form as seen in equation 38.

$$\begin{pmatrix} \hat{r} \\ \hat{\theta} \\ \hat{\phi} \end{pmatrix} = \begin{pmatrix} \sin\theta\cos\phi & \cos\theta\cos\phi & -\sin\phi \\ \sin\theta\sin\phi & \cos\theta\sin\phi & \cos\phi \\ \cos\theta & -\sin\theta & 0 \end{pmatrix} \begin{pmatrix} \hat{x} \\ \hat{y} \\ \hat{z} \end{pmatrix} \tag{38}$$

This equation can also be used to convert Cartesian vector components to spherical vector components.

## 4.2 Surface Density Plots

The first part of making surface density plots is the selection of nodes in the data. This is done fairly easily by saving the indices of the matrix locations which have the presence of a node, which is indicated by a $1$ in the matrix for nodes. Thereafter we make use of the following method:

**Method to make surface density plots**

1. Select a node (This will be the center of the plot).
2. Choose a radius, and select a data-cube around the node with length 2 times the radius.
3. Define Cartesian coordinates for each grid-point in the data-cube and take the origin to be the location of the selected node.
4. Convert all Cartesian coordinates to spherical coordinates using the method described in section 4.1.
5. Filter the data by checking if the value for $r$ is smaller than the selected radius and if this is the case store the data. This will result in a sphere of data.
6. Plot the value of every point (1 or 0) in a $\theta$ versus $\phi$ plot with Mollweide projection, we ignore the values of $r$.
7. Use the kernel density [a] to make a surface density plot of $\theta$ versus $\phi$ with Mollweide projection.

[a] Used the gaussian_kde function from the scipy.stats module.

This method is applied to the data set of only the filaments and a data set of all particles.

## 4.3 Velocity and Moment plots

Next to making surface density plots, we will also look at the radial velocity component of the particles and this component multiplied with the density at each point. We do this using the first 5 steps of the method to make surface density plots and then we need to add some steps. These steps are shown in the frame below:

**Method to make radial velocity and moment plots**

1. Follow steps 1 till 5 from the method in section 4.2
2. Calculate at each data point the radial velocity component
3. Calculate at each data point the product of the density and the radial velocity component.
4. Plot the radial velocity in a $\theta$ versus $\phi$ Mollweide projection plot. (This is done with a red-blue color map in order to see red- and blue shift.)
5. Plot also the moment in a $\theta$ versus $\phi$ Mollweide projection plot.

These plots will be made with the density field and the velocity field instead of with the particle data sets as done for the surface density plots.

## 4.4 Spherical Harmonics

The last part of the project consists of identifying spherical harmonics in the radial velocity plots and the moment plots. We identify these multi-pole patterns using the Laplace series and the inverse of the Laplace series. All mathematical background methods are described in section 3. The algorithm to perform these calculations is quite simple. It follows the method described below:

**Method to calculate spherical harmonics of a field**

1. First, we use the method described in section 4.3 to calculate the radial velocity- and moment- field.
2. Using these fields we calculate the coefficients of the spherical harmonics for each coordinate $(\theta, \phi)$ using equation 33.
3. The calculations described in the previous step are done for all values of m such that $|m| \leq l$.
4. The coefficients found in the previous step are now used to calculate the spherical harmonics for each coordinate $(\theta, \phi)$ using the Laplace series as given in equation 25.
5. Steps 2 to 4 are repeated to calculate the values of the spherical harmonics for different values of $l$.

6. There are Mollweide plots made for every value of $l$ combined with the previous found values, so for $l = 1$, the values for $l = 0$ and $l = 1$ are added.

7. Lastly, we also plot the residual function, which is the original field minus the found spherical harmonics.

# 5 Nodes and Filaments: The Sky view

This project consists of two main areas of focus. We will first discuss the surface density of the particle part of the filament and the surface density of all the particles when they are projected on the sky for different radii ranging from 5 Mpc to 25 Mpc at intervals of 5 Mpc.

In order to make the plots, we will look at all the nodes within the simulation. They are selected using the method described in section 4. We find 909 nodes within the simulation, when excluding the ones close to the edge of the simulation, to make sure that the amount of data is the same in every direction. The nodes are shown in the 3D plot in figure 21.

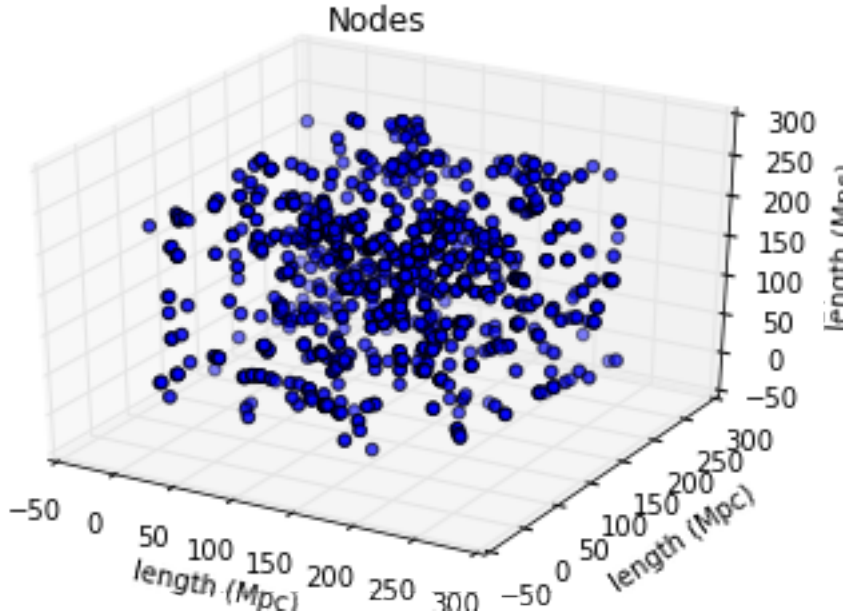


Figure 21: **Nodes** A 3D plot of all nodes in the simulation excluding the ones close to the edge of the data-box.

## 5.1 Mollweide plots

In order to show the patterns nicely, we make use of Mollweide plots. What essentially happens is that all points are projected onto a sphere and then the sphere is projected in to 2 dimensions. An example of the three-dimensional data and the resulting Mollweide plots is shown in figure 22 for two different radii.

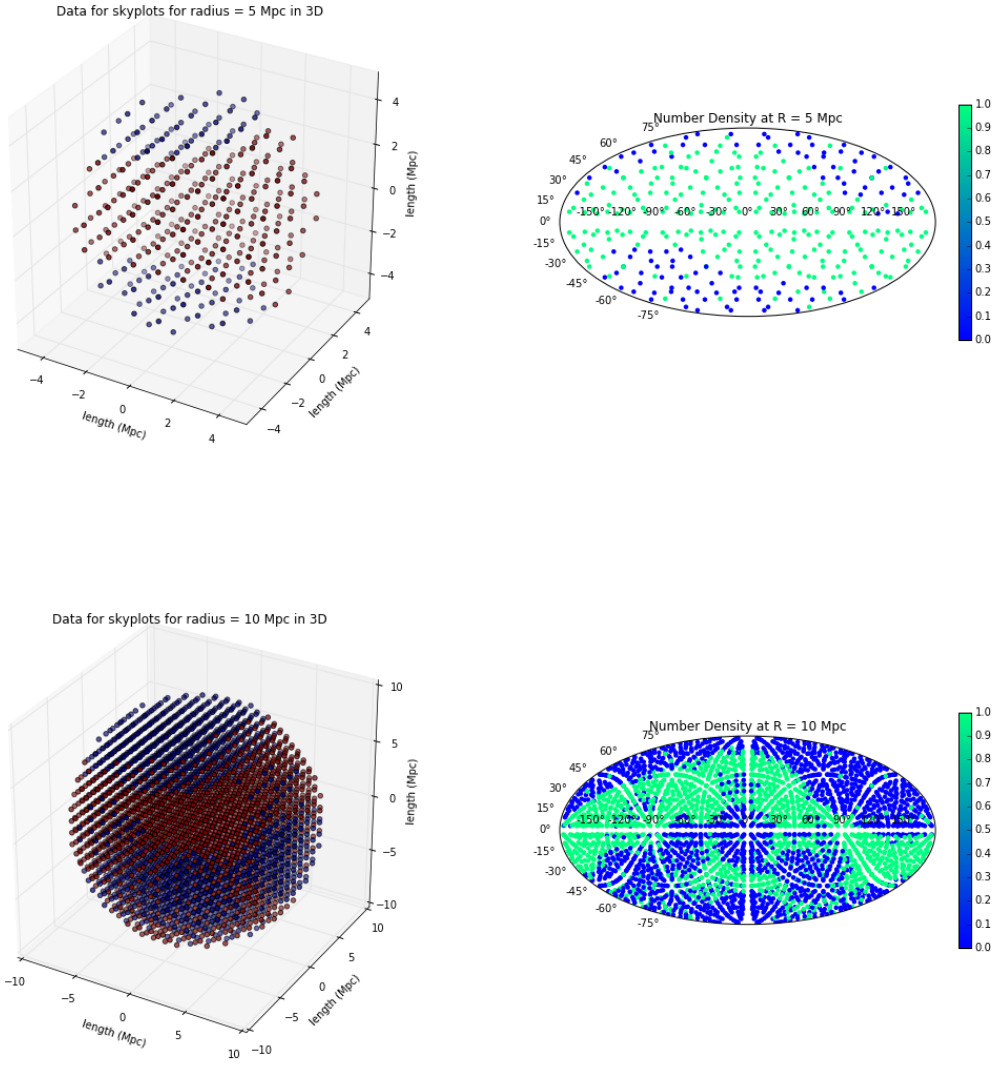


Figure 22: **3D vs Mollweide** Three dimensional data set versus the mollweide projection for 5 and 10 Mpc

## 5.2 Surface Density

For each node, we selected data within a radius $r$ and plotted the results in a Mollweide plot of the surface density. From each of these plots, we also determined the kernel density and plotted that as well for each radius. A couple of these plots for a node can be found in figures 23 and 24. Other examples can be found in the appendix in section 8.1.

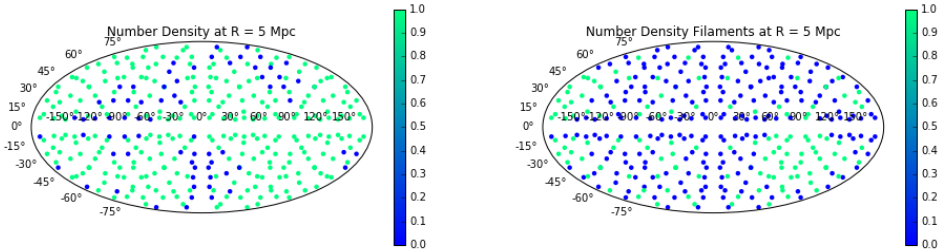


(a) Plot for the all particles (left) and the filaments (right) at a distance of 5 Mpc

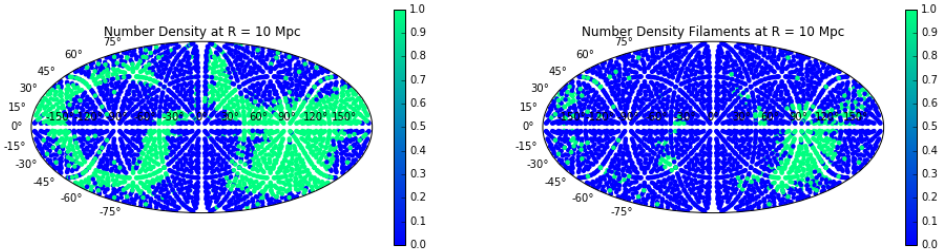


(b) Plot for the all particles (left) and the filaments (right) at a distance of 10 Mpc

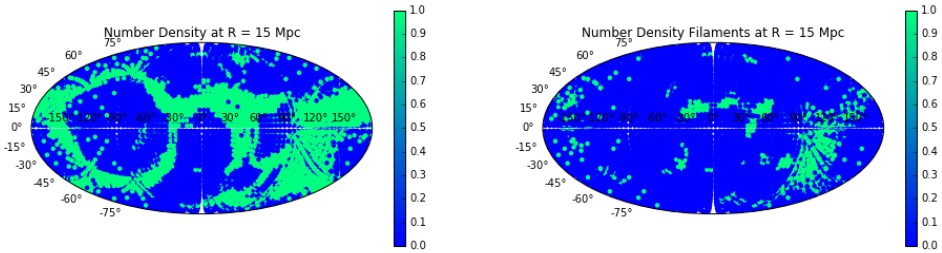


(c) Plot for the all particles (left) and the filaments (right) at a distance of 15 Mpc

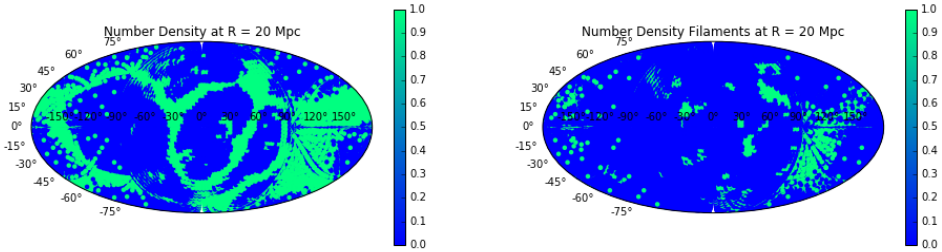


(d) Plot for the all particles (left) and the filaments (right) at a distance of 20 Mpc

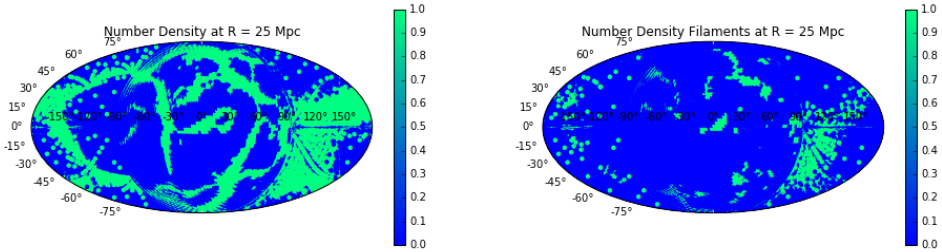


(e) Plot for the all particles (left) and the filaments (right) at a distance of 25 Mpc

Figure 23: **Surface Density** plots of the surface density.

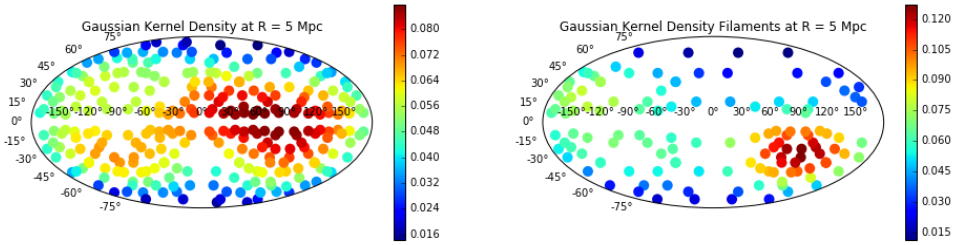


(a) Plot for the all particles (left) and the filaments (right) at a distance of 5 Mpc

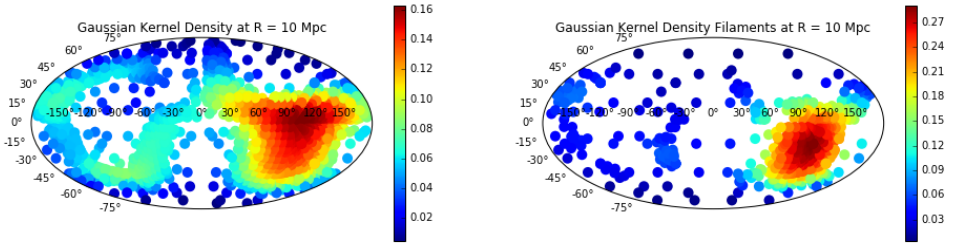


(b) Plot for the all particles (left) and the filaments (right) at a distance of 10 Mpc

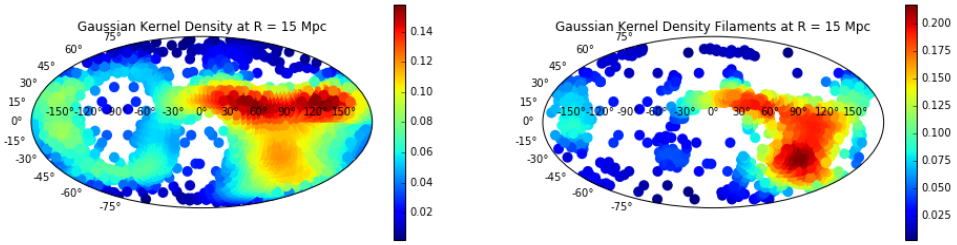


(c) Plot for the all particles (left) and the filaments (right) at a distance of 15 Mpc

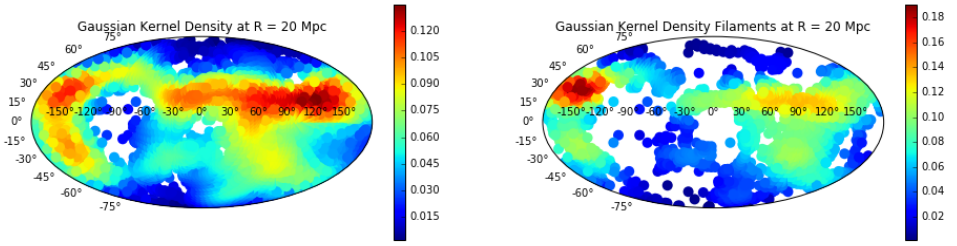


(d) Plot for the all particles (left) and the filaments (right) at a distance of 20 Mpc

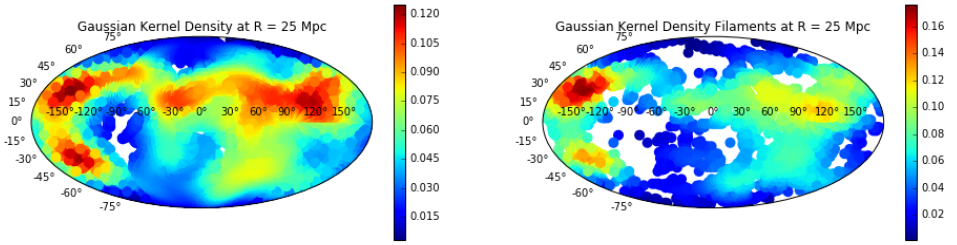


(e) Plot for the all particles (left) and the filaments (right) at a distance of 25 Mpc

Figure 24: **Surface Density** plots of the Gaussian kernel surface density.

We can calculate an average for the relative surface density for each of the nodes, with respect to all particles and with respect to the particles within the filaments. The average values with their standard deviation is shown in table 2.

Table 2: Table with the average values for the relative surface density

| **Distance (Mpc)** | **Average for all particles** | **Standard deviation all particles** | **Average for filament particles** | **Standard deviation filament particles** |
|---|---|---|---|---|
| 5 | 0.743 | 0.100 | 0.387 | 0.114 |
| 10 | 0.445 | 0.063 | 0.143 | 0.034 |
| 15 | 0.364 | 0.054 | 0.102 | 0.021 |
| 20 | 0.327 | 0.050 | 0.088 | 0.018 |
| 25 | 0.307 | 0.046 | 0.080 | 0.015 |

This table clearly indicates that the most surface density is contained in the nodes, the further we move outwards, the less the relative surface density becomes and we also see that the further we move out, the smaller the contingent of the filaments is.

# 6 Filaments and Inflow

The second main focus was the determination of flow around the nodes. First, we calculate the radial component of the velocity for every point and the momentum by multiplying the velocity by the density field. For this part of the project, we looked at a distance of 10 Mpc in order to have a contained data set which is still able to tell us something about the node.

## 6.1 Velocity and Momentum Plots

We first plotted the radial component of the velocity and the momentum. These plots are shown for a couple of nodes in figure 28.

The plots on the right in figure 28 show the radial velocity field. The red in the figures indicate a negative velocity component which means that the particles are moving away from the node. The blue in the figures indicates a positive velocity, which means that the particles are moving away from the node.

After this, we look at the density field times the radial component of the velocity. This can be seen as the momentum of the particles and thus describe the inflow and outflow from the node. The average inflow or outflow for each node is calculated of which an average and a standard deviation is calculated. We find that on average for the radial velocity field the flow is positive, namely: $63.5 \pm 16.3$ km/s. This means that the particles are moving towards the nodes as expected because of gravity. For the momentum flow, we also find a positive value, which makes sense since the velocity component is positive. The value is found to be $215.2 \pm 70.5$ km/s/kg.

## 6.2 Spherical Harmonics

Lastly, we have looked at some analysis of the previous plots by determining the spherical harmonics up to a degree of $l = 2$. We determined the average deviation from the original field and determined which value or which combination of values of $l$ described the original field best.

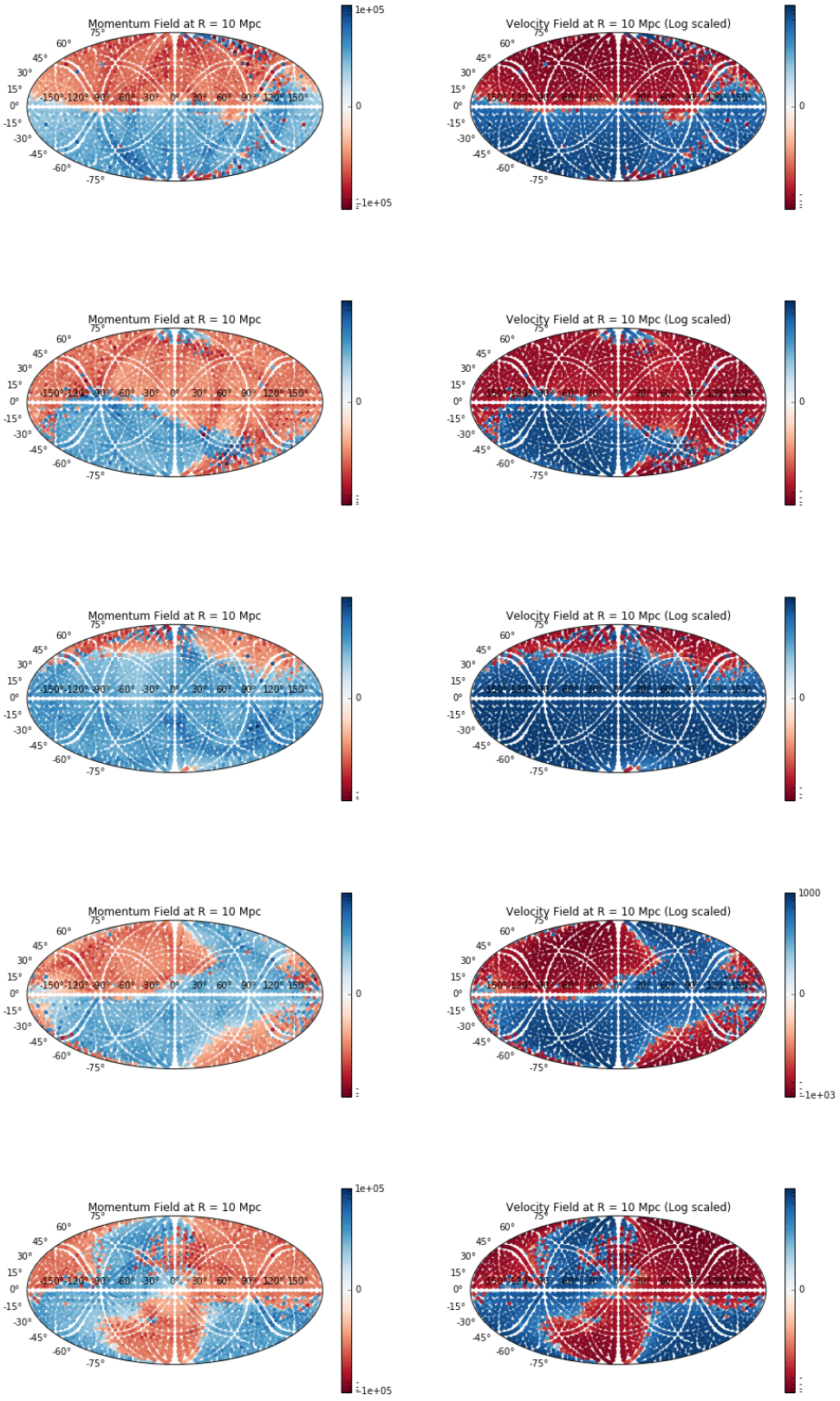


Figure 25: **Velocity and momentum field** Plots for the logarithmic velocity and momentum field at a distance of 10 Mpc.

### 6.2.1 Monopole, dipole or tripole

For every node, we determined the classification into monopole, dipole, or tripole. This is done by finding the classification with the smallest deviation with respect to the average of the field. The classification can also be a combination of a monopole and a dipole or a monopole, dipole, and tripole. The results can be found in table 3.

| classification | frequency | percentage |
|---|---|---|
| monopole | 0 | 0 |
| dipole | 28 | 4 |
| tripole | 247 | 38 |
| monopole + dipole | 27 | 4 |
| monopole + dipole + tripole | 343 | 53 |

Table 3: Classification of the nodes

### 6.2.2 Deviations

We also determined the best average deviation for all nodes. The results are shown in figure 26. The values are relative, which means that we have divided the absolute deviation by the absolute average of the field. We see that most fields have a relative average of 0.46, this means that the fits are not perfect, but they are acceptable.

We can explain the large deviation by the fact that the plots are not symmetric in the positive and negative values, which means that the absolute value of the maximum and minimum is not the same, which implies that they cannot be described by a single amplitude. Adding the $l = 3$ plot will increase the accuracy of the classification of 8 percent of the nodes. Even adding more spherical harmonics, such as $l = 4$ or even higher values for $l$ will decrease the deviation, but the overall patterns of the plots become clear from spherical harmonics up to a degree of $l = 2$.

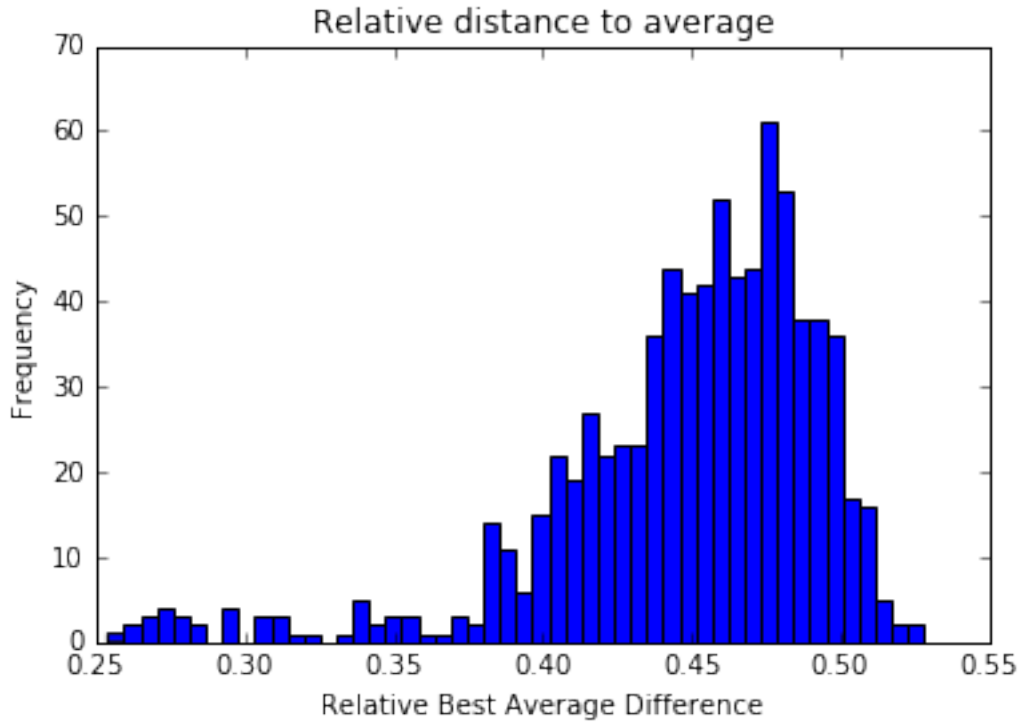


Figure 26: **Uncertainties of deviation** A histogram showing the average relative deviation of the spherical harmonics from the mean original field

### 6.2.3 Plots of the spherical harmonics for some nodes

We have selected a couple of nodes to examine in detail. These two nodes have different classification. The first node we are gonna discuss is classified to be a dipole ($l = 1$).

In figure 27 we see the original radial velocity plot for a node. In figure **??** we find the plots for $l = 1$. In figure 30 we find the plots for $l = 2$ and we find the residues for $l = 1$ and $l = 2$ in figure 29.

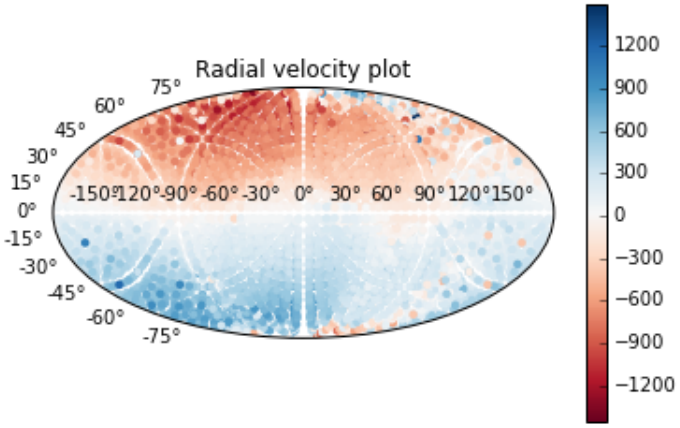


Figure 27: **Radial velocity field** The radial velocity field for a dipole node

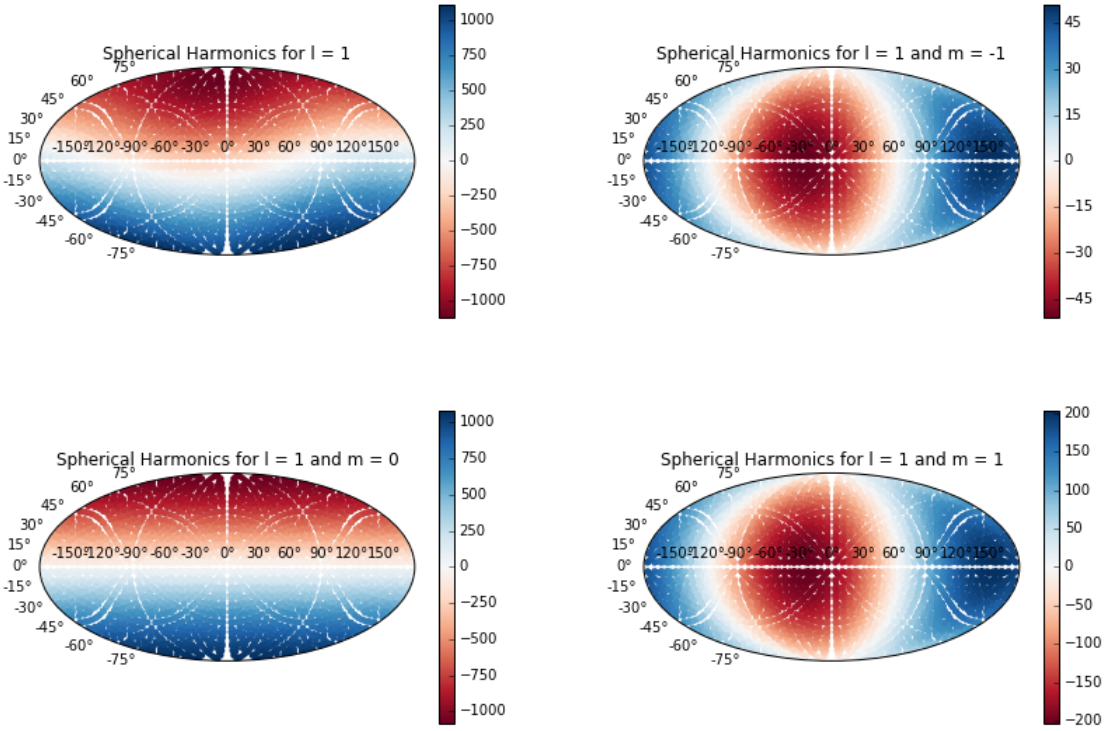


Figure 28: $l = 1$Plots of the radial velocity field for $l = 1$.

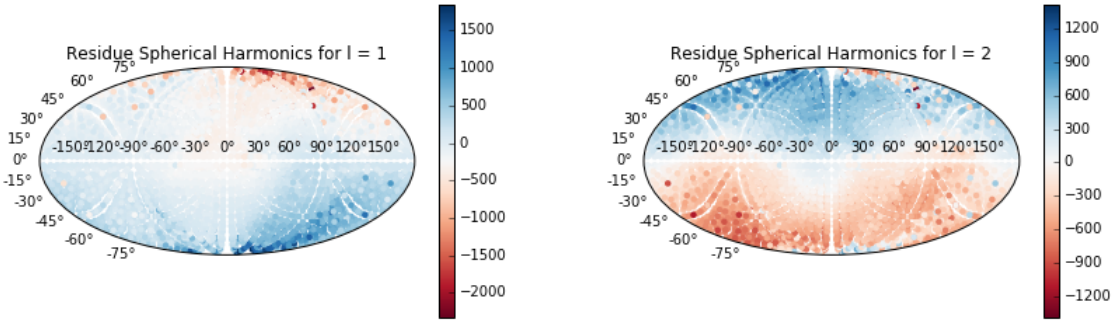


Figure 29: **Residues** The residues for the spherical harmonics of the radial velocity field.

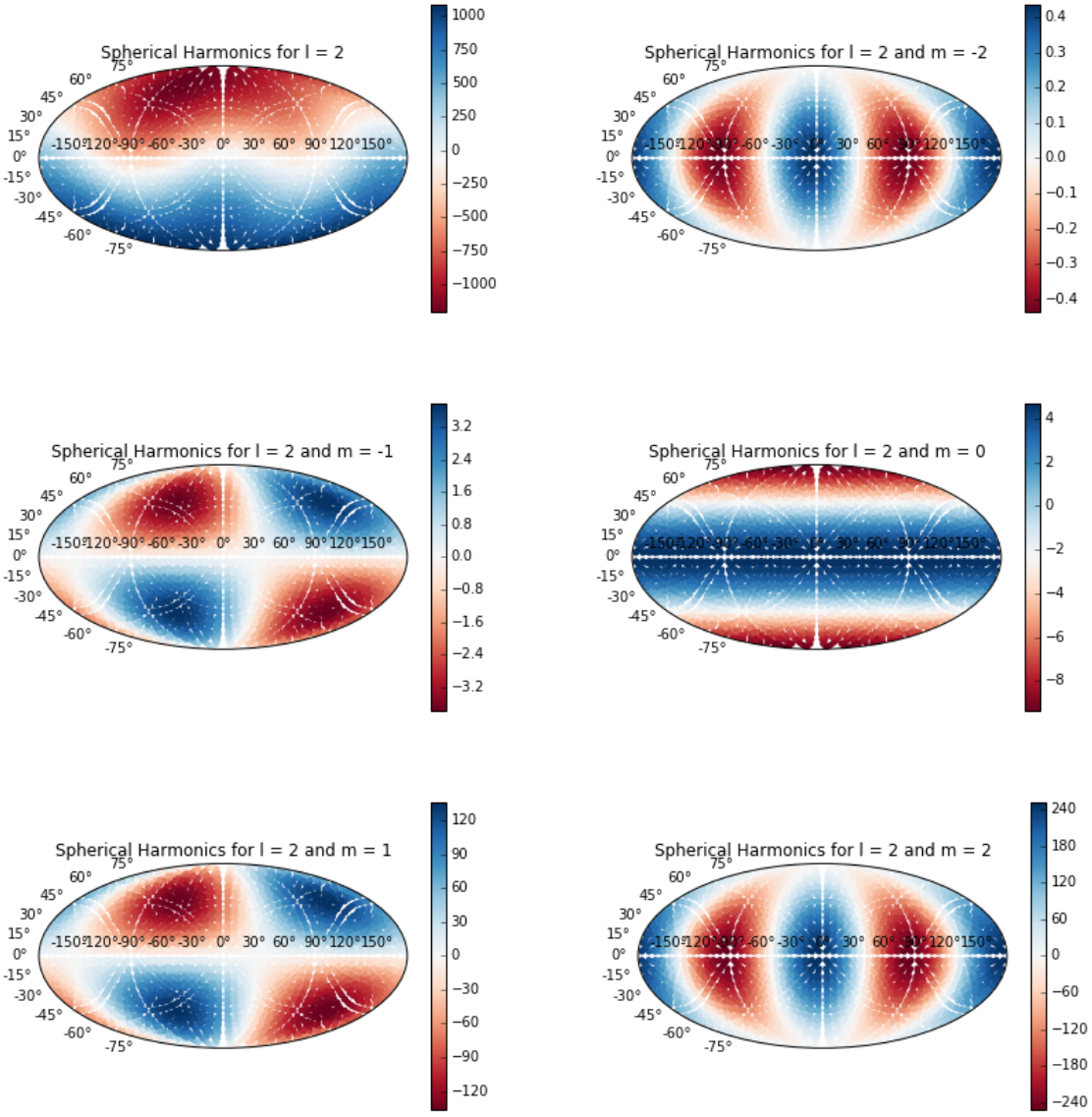


Figure 30: $l = 2$ Plots of the radial velocity field for $l = 2$.

The next node is classified as a tripole. In figure 31 we see the original radial velocity plot for a node. In figure 32 we find the plots for $l = 1$. In figure 33 we find the plots for $l = 2$ and we find the residues for $l = 1$ and $l = 2$ in figure 34.

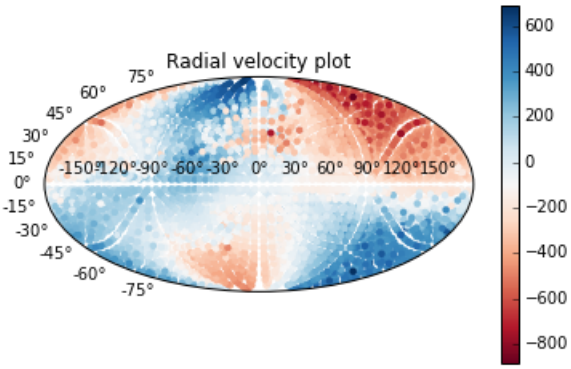


Figure 31: **Radial velocity** The radial velocity field for a dipole node

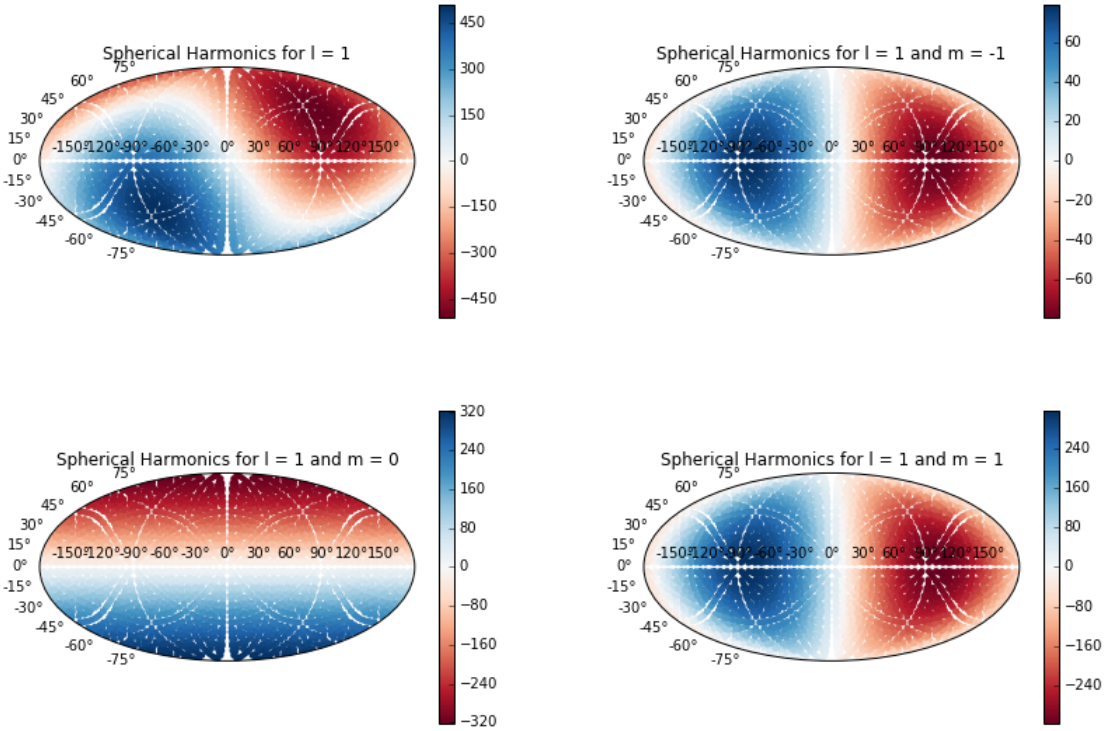


Figure 32: $l = 1$ Plots of the radial velocity field for $l = 1$.

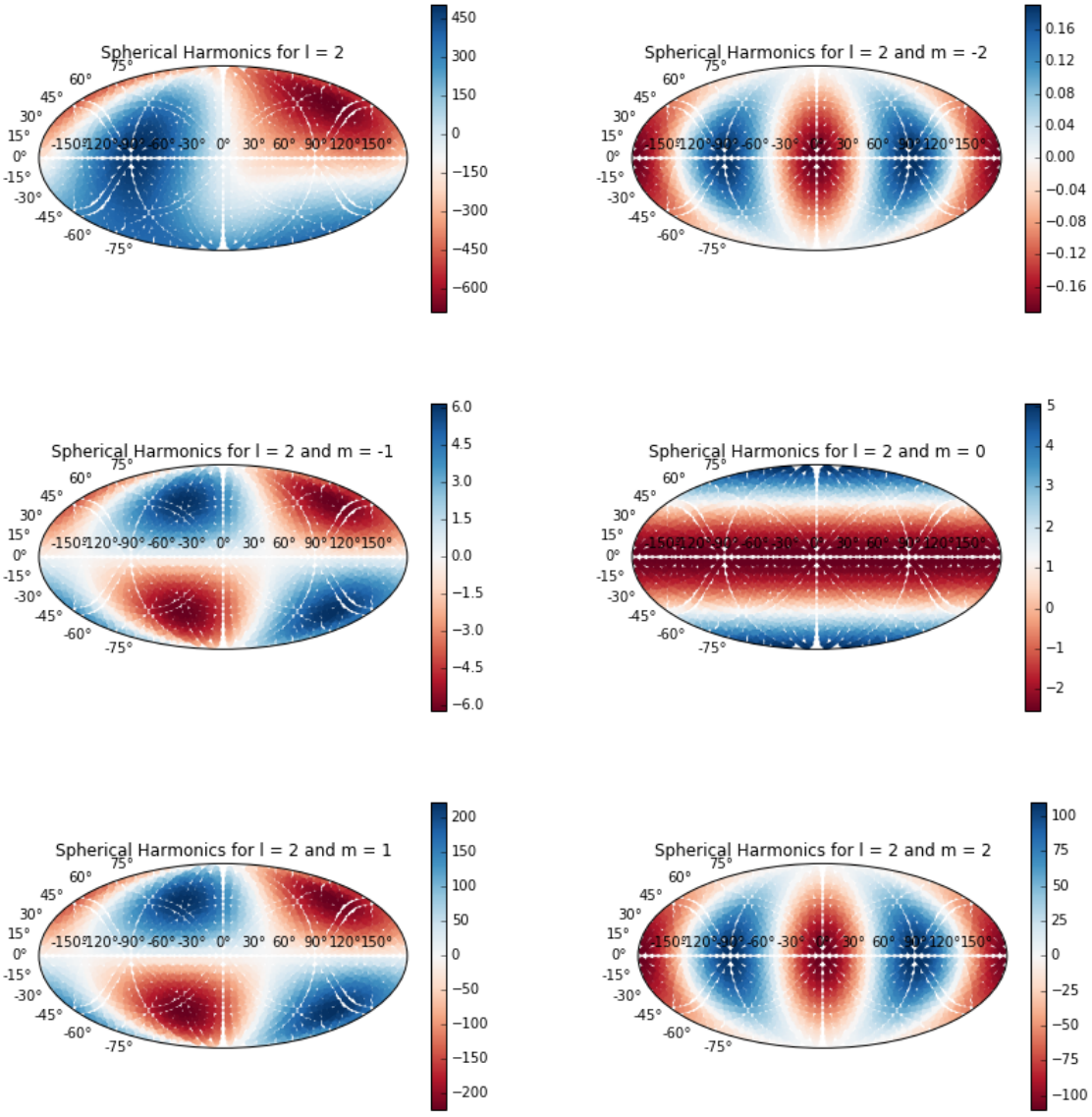


Figure 33: $l = 2$ Plots of the radial velocity field for $l = 2$.

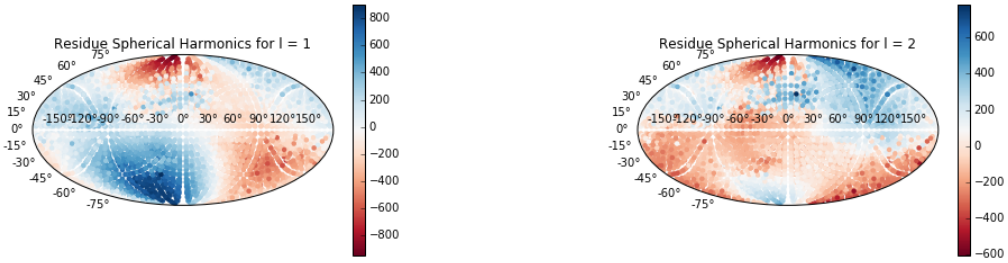


Figure 34: **Residues** The residues for the spherical harmonics of the radial velocity field.

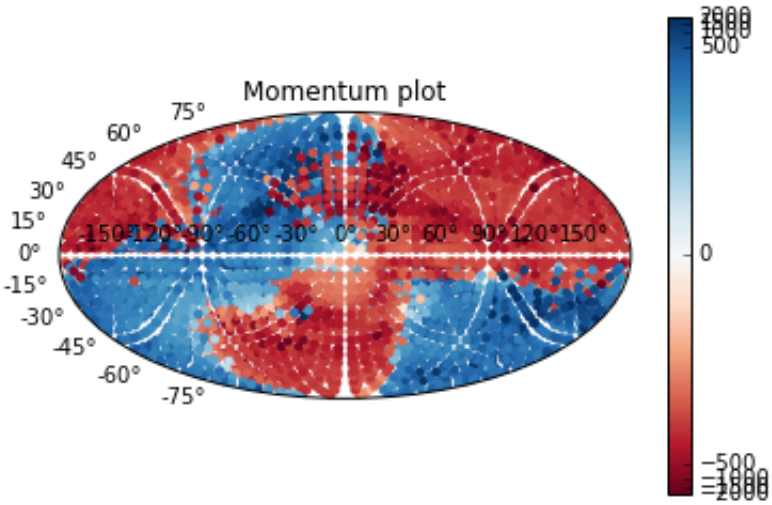


Figure 35: **Momentum field** The original momentum field

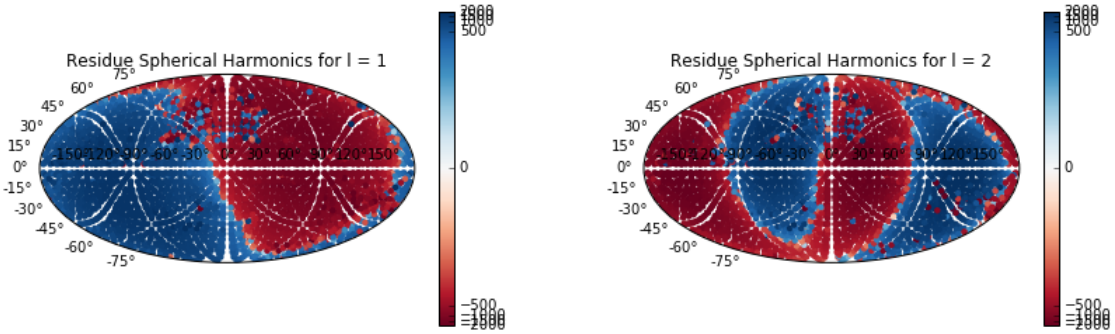


Figure 36: **Residues** The residues for the spherical harmonics of the momentum field.

### 6.2.4 Momentum Field

In figure 35 we see the original momentum field plot for a node. In figure 37 we find the plots for $l = 1$. In figure 38 we find the plots for $l = 2$ and we find the residues for $l = 1$ and $l = 2$ in figure 36.

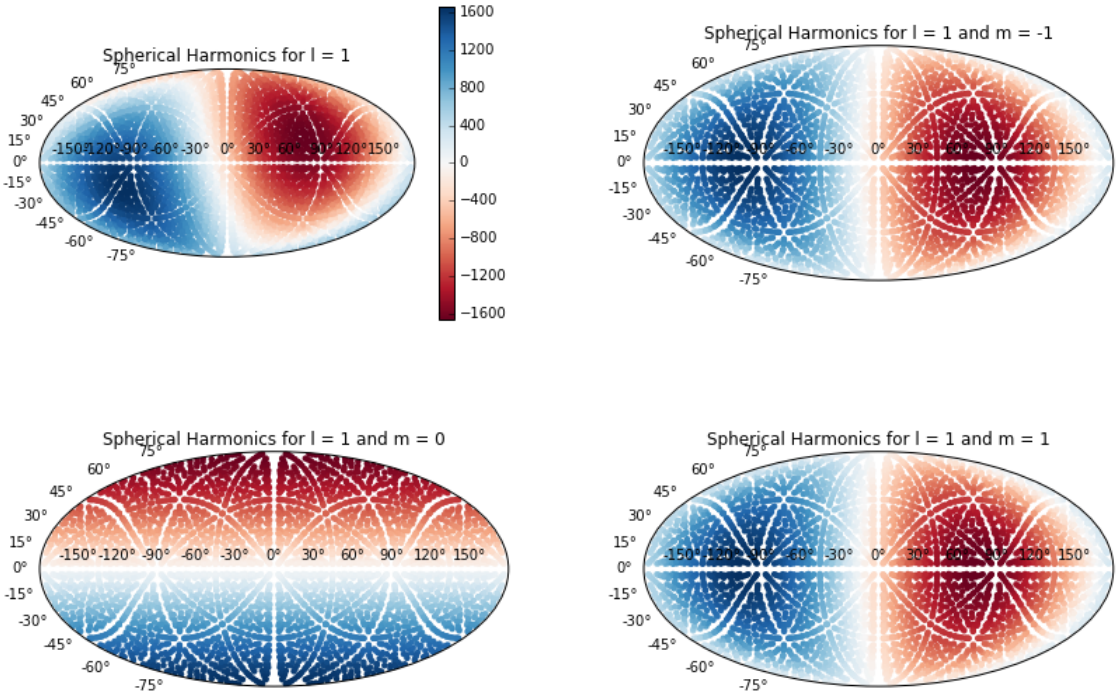


Figure 37: $l = 1$ Plots of the momentum field for $l = 1$.

We see that the fit is not really good for the momentum field. This is most likely caused by some very high values for the density at some spots in the data set which causes the spherical harmonics to fail in the first few steps. This would be corrected by higher order approximations, or it can be fixed by taking the density field and filter out the outliers.

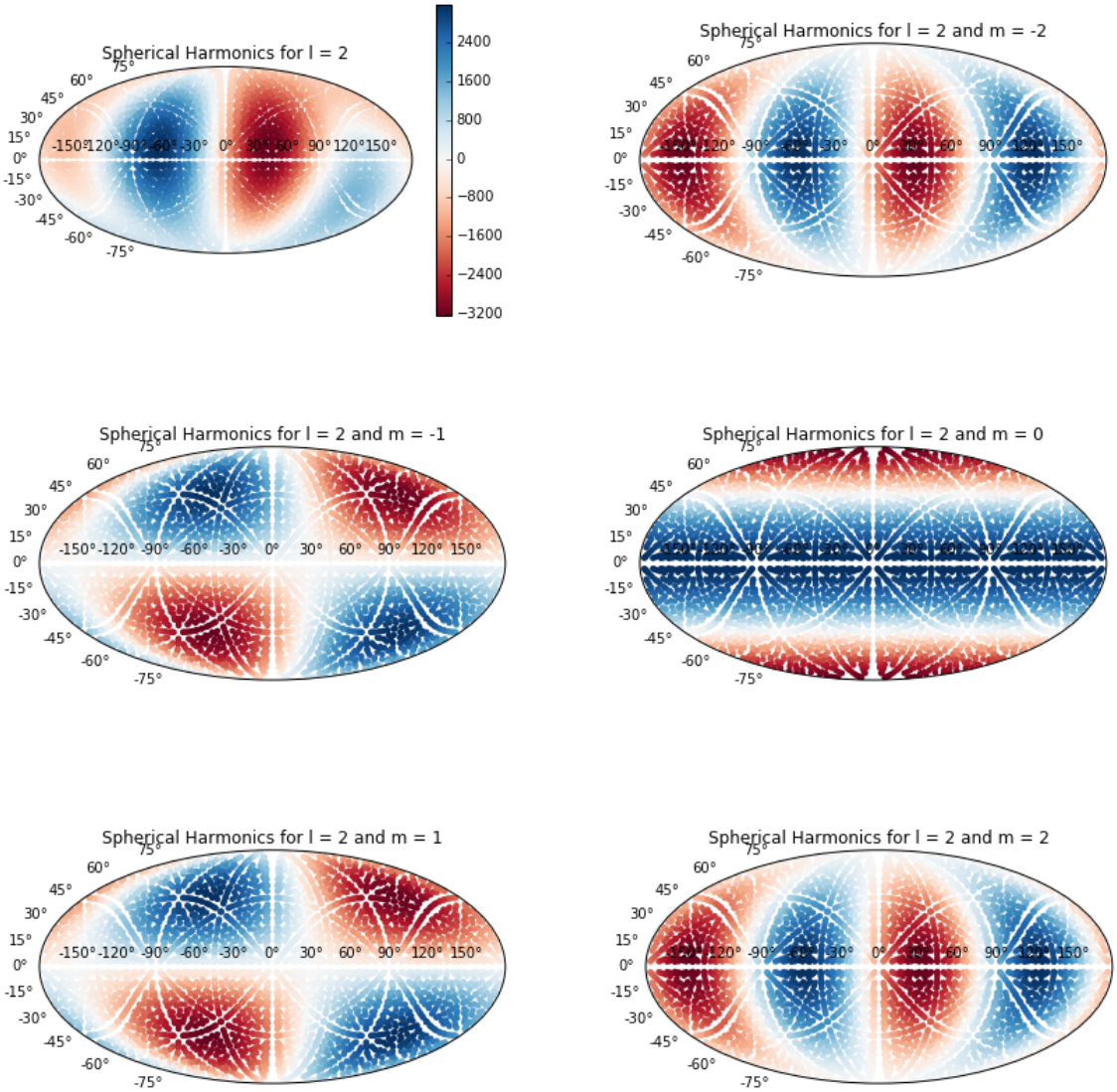


Figure 38: $l = 2$ Plots of the momentum field for $l = 2$.

# 7 Overview and Summary

The cosmic web is the largest scale structure in our universe. At this scale, we find nodes, filaments, walls, and voids. There has been done extensive research in this area, mostly relying upon simulation data. This data can be processed using an algorithm called NEXUS. There are two flavours of NEXUS, NEXUS, and NEXUS+. The main difference between these two is the way they smoothed the field. Where NEXUS uses a Gaussian filter, NEXUS+ uses the logarithmic version of the Gaussian filter and this results in a much better approximation of the real field, where a lot more structured are preserved.

After using the steps described in section 2.3, we have a data-set divided into nodes, walls and filaments. This data is used to make surface density sky plots around nodes at distances ranging from 5 megaparsec up to 25 megaparsec, increasing 5 mega parsec per step. These plots are also used to determine the Gaussian Kernel Density for each plot.

After all these steps we started looking at the velocity field, more precisely, the radial component of the velocity field. This field tells us something about the inflow and outflow of particles. We found that on average most particles were moving towards the node, which is expected based on the mass distribution in the cosmic web. We also multiplied the velocity fields with the density field around each node, in order to find the momentum flux, which tells us something about the mass displacement around the nodes. It was not surprising that we also found a positive momentum flux because of the positive radial velocity flow.

After this, we also looked at spherical harmonics. For each node we determined the best fit for the velocity- and momentum field and classified them into categories based on the best fit value for $l$. We found that most nodes can be classified as dipoles ($l = 1$). We also looked at an estimate of the uncertainty of these fits and found that they were quite large. This is most probable caused by the asymmetry of positive and negative values, but the overall pattern of the fits seem consistent with the original field. The spherical harmonics components are shown for a couple of nodes.

The results could be greatly improved by making a few adjustments and doing a couple more calculations. First of all, it would be interesting to look at some smaller scales. The simulation used for these results was a $300 \times 300 \times 300$ megaparsec box on a grid of $256 \times 256 \times 256$. It would be nice to take a smaller simulation or a bigger grid so that we would be able to look at scales of 1 megaparsec instead of 10 megaparsec. Furthermore, it would also be interesting to look at higher orders of $l$ for the spherical harmonics, in order to residues the residue and uncertainty and to find more subtle patterns in the flow around nodes.

# References


Abel, Tom, Oliver Hahn and Ralf Kaehler. 2012. "Tracing the dark matter sheet in phase space: Tracing the dark matter sheet." *Monthly Notices of the Royal Astronomical Society* 427(1):61–76.
**URL:** *https://academic.oup.com/mnras/article-lookup/doi/10.1111/j.1365-2966.2012.21754.x*

Aragon-Calvo, M. A. and A. S. Szalay. 2013. "The hierarchical structure and dynamics of voids." *Monthly Notices of the Royal Astronomical Society* 428(4):3409–3424.
**URL:** *http://academic.oup.com/mnras/article/428/4/3409/1000564/The-hierarchical-structure-and-dynamics-of-voids*

Aragon-Calvo, M. A., B. J. T. Jones, R. van de Weygaert and J. M. van der Hulst. 2007. "The multiscale morphology filter: identifying and extracting spatial patterns in the galaxy distribution." *Astronomy & Astrophysics* 474(1):315–338.
**URL:** *http://www.aanda.org/10.1051/0004-6361:20077880*

Aragon Calvo, M.A. 2007. Morphology and Dynamics of the Cosmic Web PhD thesis University of Groningen.
**URL:** *https://www.rug.nl/research/portal/files/14546044/thesis.pdf*

Aragon-Calvo, Miguel A., Erwin Platen, Rien van de Weygaert and Alexander S. Szalay. 2010. "THE SPINE OF THE COSMIC WEB." *The Astrophysical Journal* 723(1):364–382.
**URL:** *https://iopscience.iop.org/article/10.1088/0004-637X/723/1/364*

Aragon-Calvo, Miguel A., Rien Van De Weygaert and Bernard J. T. Jones. 2010. "Multiscale phenomenology of the cosmic web: Multiscale phenomenology of the cosmic web." *Monthly Notices of the Royal Astronomical Society* 408(4):2163–2187.
**URL:** *https://academic.oup.com/mnras/article-lookup/doi/10.1111/j.1365-2966.2010.17263.x*

Aragon-Calvo, Miguel A., Rien van de Weygaert, Bernard J. T. Jones and J. M. van der Hulst. 2007. "Spin Alignment of Dark Matter Halos in Filaments and Walls." *The Astrophysical Journal* 655(1):L5–L8.
**URL:** *https://iopscience.iop.org/article/10.1086/511633*

Arfken, George B. and Hans-Jurgen Weber. 2005. *Mathematical methods for physicists*. 6th ed ed. Boston: Elsevier.

Bharadwaj, Somnath, Suketu P. Bhavsar and Jatush V. Sheth. 2004. "The size of the longest

filaments in the universe." *The Astrophysical Journal* 606(1):25–31.
**URL:** *https://iopscience.iop.org/article/10.1086/382140*

Carroll, Bradley W. and Dale A. Ostlie. 2014. *An introduction to modern astrophysics*. 2. ed., pearson new internat. ed ed. Harlow: Pearson. OCLC: 868368508.

Cautun, Marius, Rien van de Weygaert and Bernard J. T. Jones. 2013. "Nexus: tracing the cosmic web connection." *Monthly Notices of the Royal Astronomical Society* 429(2):1286–1308. arXiv: 1209.2043.
**URL:** *http://arxiv.org/abs/1209.2043*

Cautun, Marius, Rien Van De Weygaert, Bernard JT Jones and Carlos S Frenk. 2014. "Evolution of the cosmic web." *Monthly Notices of the Royal Astronomical Society* 441(4):2923–2973.

Colless, Matthew, Gavin Dalton, Steve Maddox, Will Sutherland, Peder Norberg, Shaun Cole, Joss Bland-Hawthorn, Terry Bridges, Russell Cannon, Chris Collins, Warrick Couch, Nicholas Cross, Kathryn Deeley, Roberto De Propris, Simon P. Driver, George Efstathiou, Richard S. Ellis, Carlos S. Frenk, Karl Glazebrook, Carole Jackson, Ofer Lahav, Ian Lewis, Stuart Lumsden, Darren Madgwick, John A. Peacock, Bruce A. Peterson, Ian Price, Mark Seaborne, Keith Taylor and (the 2dFGRS team). 2001. "The 2dF Galaxy Redshift Survey: spectra and redshifts." *Monthly Notices of the Royal Astronomical Society* 328(4):1039–1063.
**URL:** *https://academic.oup.com/mnras/article-lookup/doi/10.1046/j.1365-8711.2001.04902.x*

Courtois, Helene M, Renee C Kraan-Korteweg, Alexandra Dupuy, Romain Graziani and Noam I Libeskind. 2019. "A kinematic confirmation of the hidden Vela supercluster." *Monthly Notices of the Royal Astronomical Society: Letters* 490(1):L57–L61.
**URL:** *https://academic.oup.com/mnrasl/article/490/1/L57/5579037*

Frangi, Alejandro F., Wiro J. Niessen, Koen L. Vincken and Max A. Viergever. 1998. Multiscale vessel enhancement filtering. In *Medical Image Computing and Computer-Assisted Intervention — MICCAI'98*, ed. William M. Wells, Alan Colchester and Scott Delp. Vol. 1496 Berlin, Heidelberg: Springer Berlin Heidelberg pp. 130–137.
**URL:** *http://link.springer.com/10.1007/BFb0056195*

Ganeshaiaha Veena, Punyakoti, Marius Cautun, Rien van de Weygaert, Elmo Tempel, Bernard J T Jones, Steven Rieder and Carlos S Frenk. 2018. "The Cosmic Ballet: spin and shape alignments of haloes in the cosmic web." *Monthly Notices of the Royal Astronomical Society* 481(1):414–438.
**URL:** *https://academic.oup.com/mnras/article/481/1/414/5076057*

Gott III, J. Richard, Mario Juric, David Schlegel, Fiona Hoyle, Michael Vogeley, Max Tegmark, Neta Bahcall and Jon Brinkmann. 2005. "A Map of the Universe." *The Astrophysical Journal* 624(2):463–484.
**URL:** *https://iopscience.iop.org/article/10.1086/428890*

Hahn, O., C. Porciani, C. M. Carollo and A. Dekel. 2007. "Properties of dark matter haloes in clusters, filaments, sheets and voids." *Monthly Notices of the Royal Astronomical Society* 375(2):489–499.
**URL:** *https://academic.oup.com/mnras/article-lookup/doi/10.1111/j.1365-2966.2006.11318.x*

Harber, Howard E. 2012. The Spherical Harmonics.
**URL:** *http://scipp.ucsc.edu/ haber/ph116C/SphericalHarmonics*$_1 2.pdf$

Hoffman, Yehuda, Daniel Pomarede, R. Brent Tully and Helene M. Courtois. 2017. "The dipole repeller." *Nature Astronomy* 1(2):0036.
**URL:** *http://www.nature.com/articles/s41550-016-0036*

Jones, Bernard J. T. and Rien van de Weygaert. 2014. "The structural elements of the cosmic web." *Proceedings of the International Astronomical Union* 11(S308):219–235. arXiv: 1611.01217.
**URL:** *http://arxiv.org/abs/1611.01217*

Jones, Bernard J. T., Rien Van De Weygaert and Miguel A. Aragon-Calvo. 2010. "Fossil evidence for spin alignment of Sloan Digital Sky Survey galaxies in filaments: Spin alignment of SDSS galaxies in filaments." *Monthly Notices of the Royal Astronomical Society* 408(2):897–918.
**URL:** *https://academic.oup.com/mnras/article-lookup/doi/10.1111/j.1365-2966.2010.17202.x*

Kirshner, Robert P. 2002. *The extravagant universe: exploding stars, dark energy, and the accelerating cosmos*. Princeton, N.J: Princeton University Press.

Klypin, Anatoly, Joel Primack and S. Cantalupo. N.d.
**URL:** *http://hipacc.ucsc.edu/Bolshoi.html*

Kornilov, Anton and Ilia Safonov. 2018. "An Overview of Watershed Algorithm Implementations in Open Source Libraries." *Journal of Imaging* 4(10):123.
**URL:** *http://www.mdpi.com/2313-433X/4/10/123*

Kraljic, Katarina, Christophe Pichon, Sandrine Codis, Clotilde Laigle, Romeel Dave, Yohan Dubois, Ho Seong Hwang, Dmitri Pogosyan, Stephane Arnouts, Julien Devriendt, Marcello Musso, Sebastien Peirani, Adrianne Slyz and Marie Treyer. 2020. "The impact of the connectivity of the cosmic web on the physical properties of galaxies at its nodes." *Monthly Notices of*

*the Royal Astronomical Society* 491(3):4294–4309.
**URL:** *https://academic.oup.com/mnras/article/491/3/4294/5644438*

Libeskind, Noam I, Rien Van De Weygaert, Marius Cautun, Bridget Falck, Elmo Tempel, Tom Abel, Mehmet Alpaslan, Miguel A Aragón-Calvo, Jaime E Forero-Romero, Roberto Gonzalez et al. 2018. "Tracing the cosmic web." *Monthly Notices of the Royal Astronomical Society* 473(1):1195–1217.

Lynden-Bell, D., S. M. Faber, David Burstein, Roger L. Davies, Alan Dressler, R. J. Terlevich and Gary Wegner. 1988. "Spectroscopy and photometry of elliptical galaxies. V - Galaxy streaming toward the new supergalactic center." *The Astrophysical Journal* 326:19.
**URL:** *http://adsabs.harvard.edu/doi/10.1086/166066*

Neyrinck, Mark C. 2008. "ZOBOV: a parameter-free void-finding algorithm." *Monthly Notices of the Royal Astronomical Society* 386(4):2101–2109. arXiv: 0712.3049.
**URL:** *http://arxiv.org/abs/0712.3049*

Peebles, P. J. E. 1980. *The large-scale structure of the universe*. Princeton series in physics Princeton, N.J: Princeton University Press.

Platen, Erwin, Rien van de Weygaert and Bernard J. T. Jones. 2008. "Alignment of voids in the cosmic web." *Monthly Notices of the Royal Astronomical Society* 387(1):128–136.
**URL:** *https://academic.oup.com/mnras/article-lookup/doi/10.1111/j.1365-2966.2008.13019.x*

Proust, D., H. Quintana, E. R. Carrasco, A. Reisenegger, E. Slezak, H. Muriel, R. Dunner, L. Sodre, M. J. Drinkwater, Q. A. Parker and C. J. Ragone. 2006. "Structure and dynamics of the Shapley Supercluster: Velocity catalogue, general morphology and mass." *Astronomy & Astrophysics* 447(1):133–144.
**URL:** *http://www.aanda.org/10.1051/0004-6361:20052838*

Rieder, Steven, Rien Van De Weygaert, Marius Cautun, Burcu Beygu and Simon Portegies Zwart. 2013. "Assembly of filamentary void galaxy configurations." *Monthly Notices of the Royal Astronomical Society* 435(1):222–241.

Rieder, Van de Weijgaert and Portegies-Zwart. 2020.

Romano-Diaz, Emilio and Rien van de Weygaert. 2007. "Delaunay Tessellation Field Estimator analysis of the PSCz local Universe: density field and cosmic flow." *Monthly Notices of the Royal Astronomical Society* 382(1):2–28.

Sato, Yoshinobu, Shin Nakajima, Nobuyuki Shiraga, Hideki Atsumi, Shigeyuki Yoshida, Thomas Koller, Guido Gerig and Ron Kikinis. 1998. "Three-dimensional multi-scale line filter for seg-

mentation and visualization of curvilinear structures in medical images." *Medical Image Analysis* 2(2):143–168.
**URL:** *https://linkinghub.elsevier.com/retrieve/pii/S1361841598800091*

Shapley, Harlow. 1930. "Note on a Remote Cloud of Galaxies in Centaurus." *Harvard College Observatory Bulletin* 874:9–12.

Sheth, Ravi K, HJ Mo and Giuseppe Tormen. 2001. "Ellipsoidal collapse and an improved model for the number and spatial distribution of dark matter haloes." *Monthly Notices of the Royal Astronomical Society* 323(1):1–12.

Sheth, Ravi K. and Rien van de Weygaert. 2004. "A hierarchy of voids: Much ado about nothing." *Monthly Notices of the Royal Astronomical Society* 350(2):517–538. arXiv: astro-ph/0311260.
**URL:** *http://arxiv.org/abs/astro-ph/0311260*

Sousbie, T., C. Pichon and H. Kawahara. 2011. "The persistent cosmic web and its filamentary structure - II. Illustrations: Persistent cosmic web - II: Illustrations." *Monthly Notices of the Royal Astronomical Society* 414(1):384–403.
**URL:** *https://academic.oup.com/mnras/article-lookup/doi/10.1111/j.1365-2966.2011.18395.x*

*Spherical Harmonics*. N.d.
**URL:** *https://www.researchgate.net/figure/Spherical-harmonics-by-order-columns-left-to-right-and-degree-rows-bottom-to*$_{fig}18_51548818$

Springel, Volker, Simon D. M. White, Adrian Jenkins, Carlos S. Frenk, Naoki Yoshida, Liang Gao, Julio Navarro, Robert Thacker, Darren Croton, John Helly, John A. Peacock, Shaun Cole, Peter Thomas, Hugh Couchman, August Evrard, JÃ¶rg Colberg and Frazer Pearce. 2005. "Simulations of the formation, evolution and clustering of galaxies and quasars." *Nature* 435(7042):629–636.
**URL:** *http://www.nature.com/articles/nature03597*

Tempel, E., A. Tamm, M. Gramann, T. Tuvikene, L. J. Liivamagi, I. Suhhonenko, R. Kipper, M. Einasto and E. Saar. 2014. "Flux- and volume-limited groups/clusters for the SDSS galaxies: catalogues and mass estimation." *Astronomy & Astrophysics* 566:A1. arXiv: 1402.1350.
**URL:** *http://arxiv.org/abs/1402.1350*

Tempel, E., R. S. Stoica, V. J. Martinez, L. J. Liivamagi, G. Castellan and E. Saar. 2014. "Detecting filamentary pattern in the cosmic web: a catalogue of filaments for the SDSS." *Monthly Notices of the Royal Astronomical Society* 438(4):3465–3482.
**URL:** *http://academic.oup.com/mnras/article/438/4/3465/1107139/Detecting-filamentary-pattern-in-the-cosmic-web-a*

Tully, R Brent, Helene Courtois, Yehuda Hoffman and Daniel Pomarède. 2014. "The Laniakea supercluster of galaxies." *Nature* 513(7516):71–73.

Tully, R Brent, Hélène M Courtois and Jenny G Sorce. 2016. "COSMICFLOWS-3." *The Astronomical Journal* 152(2):50.

Van de Weijgaert, Rien and J. Richard Bond. 2005. Observations and Morphology of the Cosmic Web.
**URL:** *https://www.astro.rug.nl/ weygaert/tim1publication/weybondgh2005.paper2.pdf*

van de Weygaert, Rien. 2014. "Voids and the Cosmic Web: cosmic depression & spatial complexity." *Proceedings of the International Astronomical Union* 11(S308):493–523.
**URL:** *https://www.cambridge.org/core/product/identifier/S1743921316010504/type/journal*$_article$

Van De Weygaert, Rien and Erwin Platen. 2011. "COSMIC VOIDS: STRUCTURE, DYNAMICS AND GALAXIES." *International Journal of Modern Physics: Conference Series* 01:41–66.
**URL:** *https://www.worldscientific.com/doi/abs/10.1142/S2010194511000092*

van Haarlem, Michiel and Rien van de Weygaert. 1993. "Velocity Fields and Alignments of Clusters in Gravitational Instability Scenarios." *The Astrophysical Journal* 418:544.
**URL:** *http://adsabs.harvard.edu/doi/10.1086/173416*

Villumsen, JV and M Davis. 1986. "Velocity fields around rich clusters of galaxies." *The Astrophysical Journal* 308:499–509.

White, Martin. 2014. "The Zel'dovich approximation." *Monthly Notices of the Royal Astronomical Society* 439(4):3630–3640.
**URL:** *http://academic.oup.com/mnras/article/439/4/3630/1160173/The-Zeldovich-approximation*

White, SIMON DM and JOSEPH Silk. 1979. "The growth of aspherical structure in the universe-Is the local supercluster an unusual system." *The Astrophysical Journal* 231:1–9.

Zel'Dovich, Ya B. 1970. "Gravitational instability: An approximate theory for large density perturbations." *Astronomy and astrophysics* 5:84–89.

# 8 Appendix

## 8.1 Surface Density plots

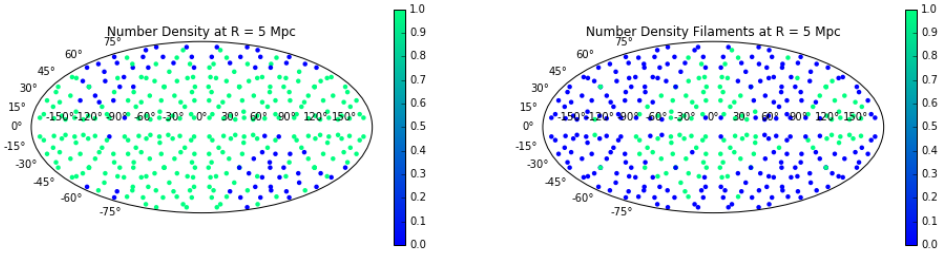


(a) Plot for the all particles (left) and the filaments (right) at a distance of 5 Mpc

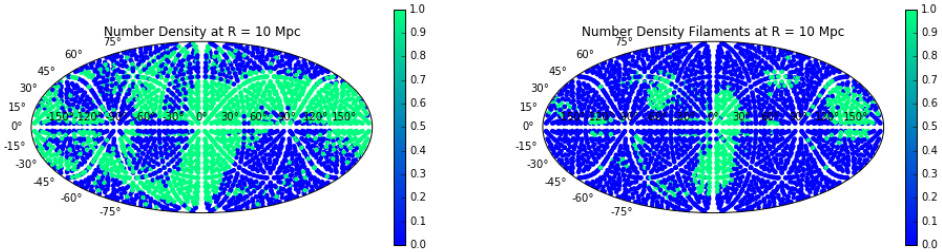


(b) Plot for the all particles (left) and the filaments (right) at a distance of 10 Mpc

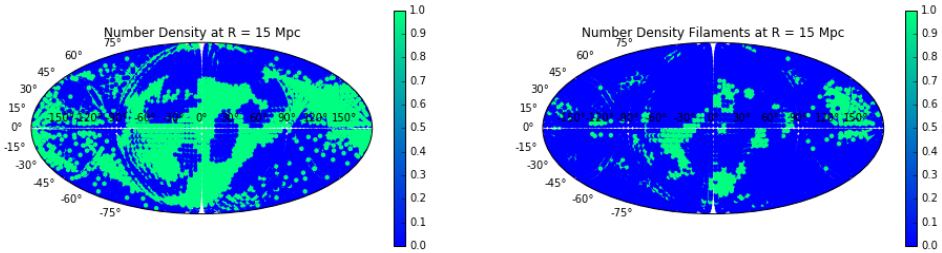


(c) Plot for the all particles (left) and the filaments (right) at a distance of 15 Mpc

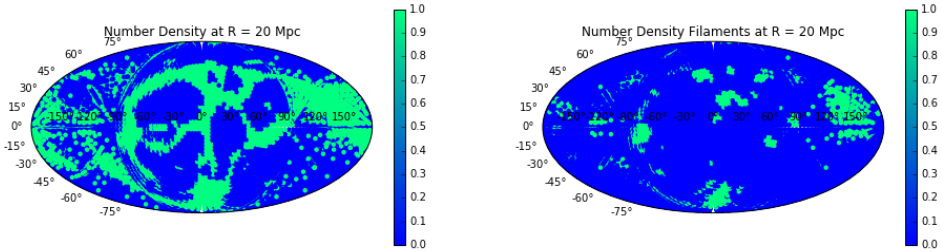


(d) Plot for the all particles (left) and the filaments (right) at a distance of 20 Mpc

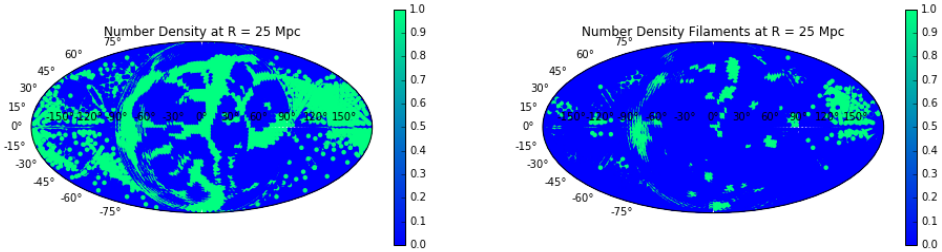


(e) Plot for the all particles (left) and the filaments (right) at a distance of 25 Mpc

Figure 39: plots of the surface density.

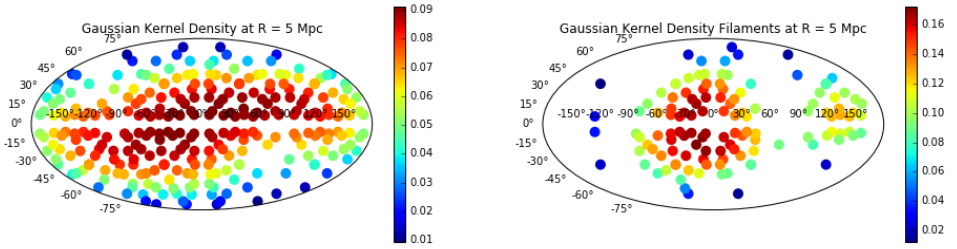


(a) Plot for the all particles (left) and the filaments (right) at a distance of 5 Mpc

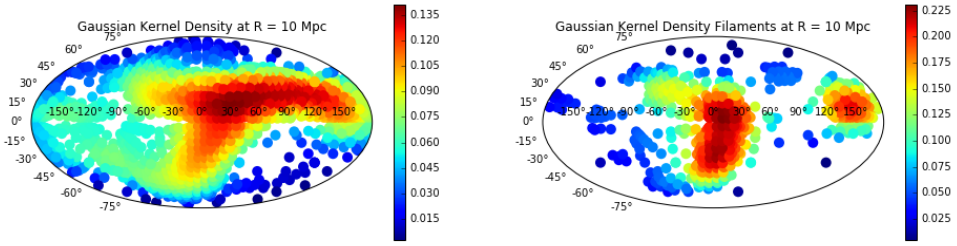


(b) Plot for the all particles (left) and the filaments (right) at a distance of 10 Mpc

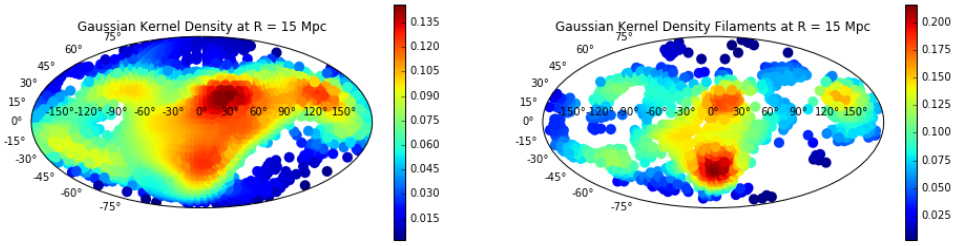


(c) Plot for the all particles (left) and the filaments (right) at a distance of 15 Mpc

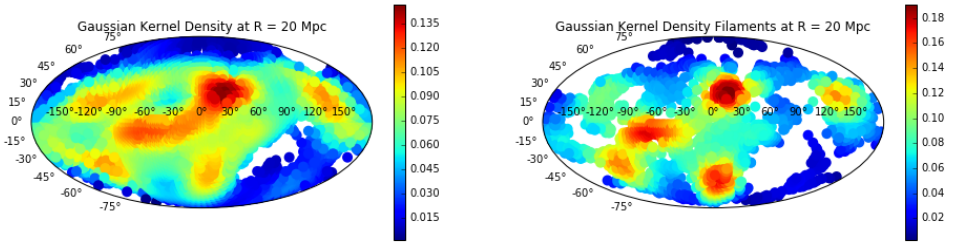


(d) Plot for the all particles (left) and the filaments (right) at a distance of 20 Mpc

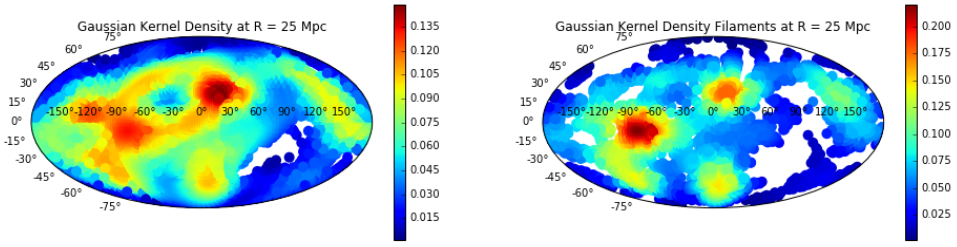


(e) Plot for the all particles (left) and the filaments (right) at a distance of 25 Mpc

Figure 40: plots of the surface density.

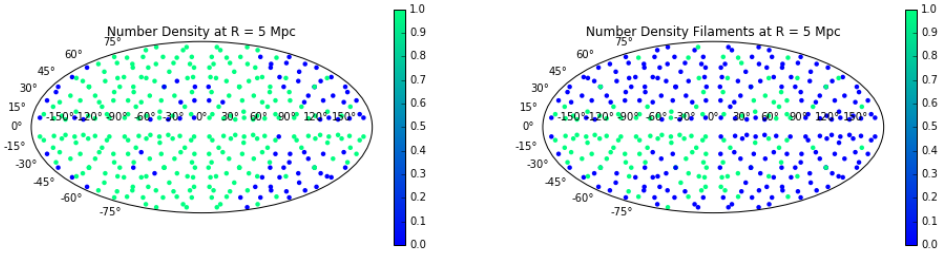


(a) Plot for the all particles (left) and the filaments (right) at a distance of 5 Mpc

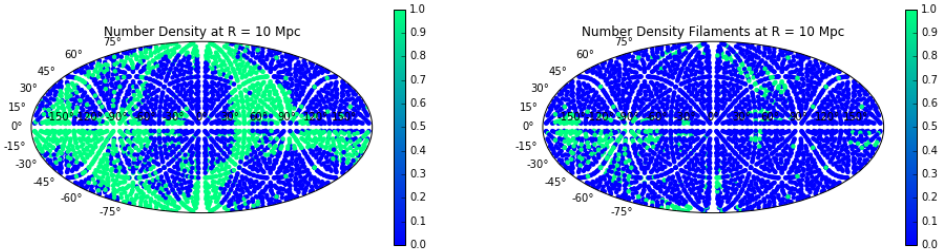


(b) Plot for the all particles (left) and the filaments (right) at a distance of 10 Mpc

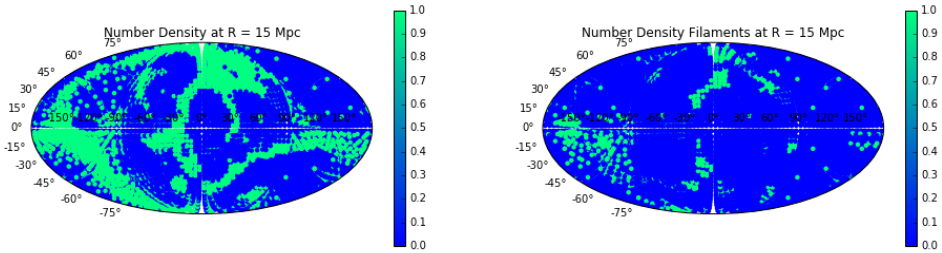


(c) Plot for the all particles (left) and the filaments (right) at a distance of 15 Mpc

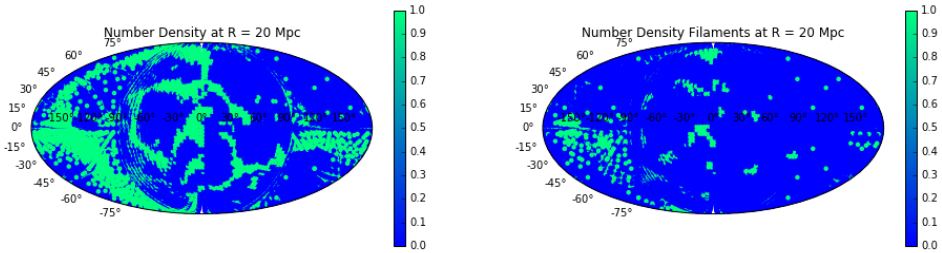


(d) Plot for the all particles (left) and the filaments (right) at a distance of 20 Mpc

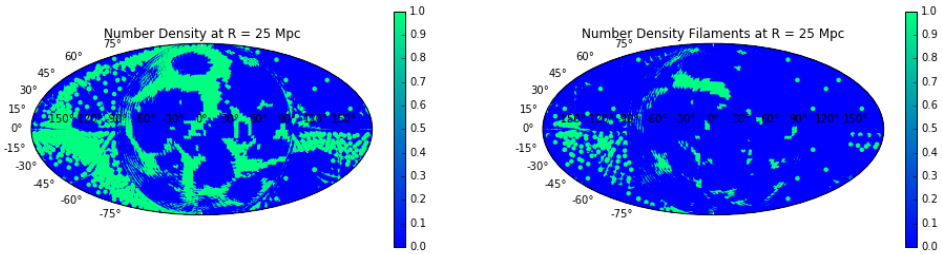


(e) Plot for the all particles (left) and the filaments (right) at a distance of 25 Mpc

Figure 41: plots of the surface density.

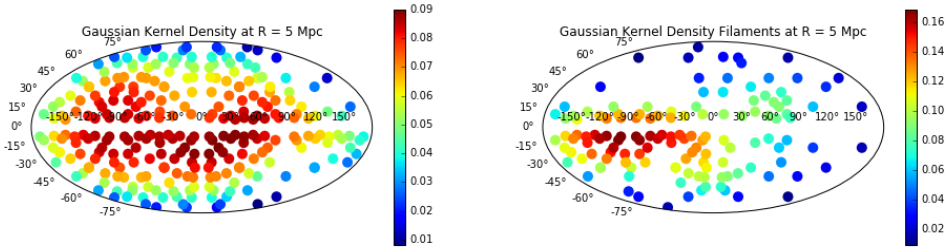


(a) Plot for the all particles (left) and the filaments (right) at a distance of 5 Mpc

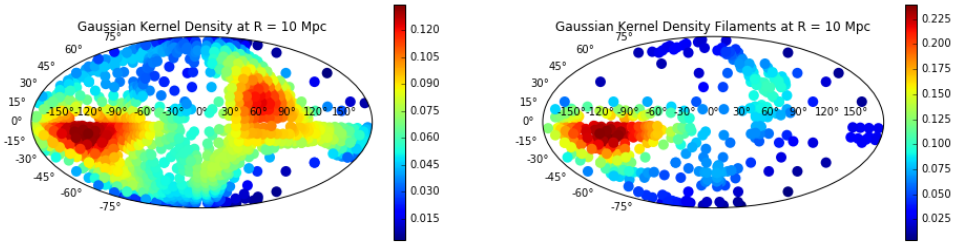


(b) Plot for the all particles (left) and the filaments (right) at a distance of 10 Mpc

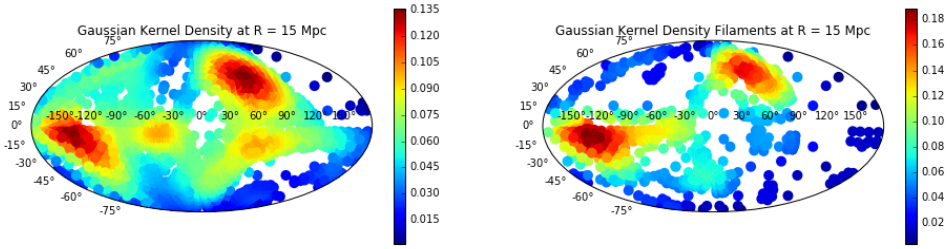


(c) Plot for the all particles (left) and the filaments (right) at a distance of 15 Mpc

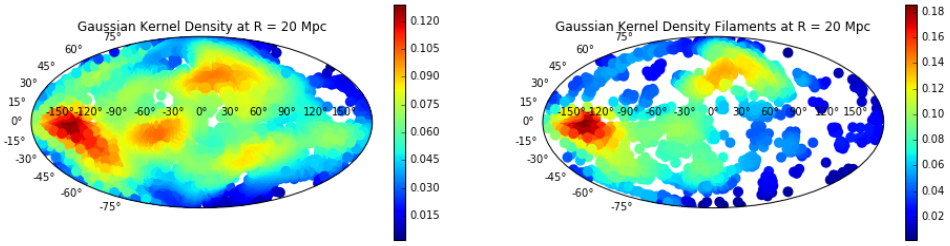


(d) Plot for the all particles (left) and the filaments (right) at a distance of 20 Mpc

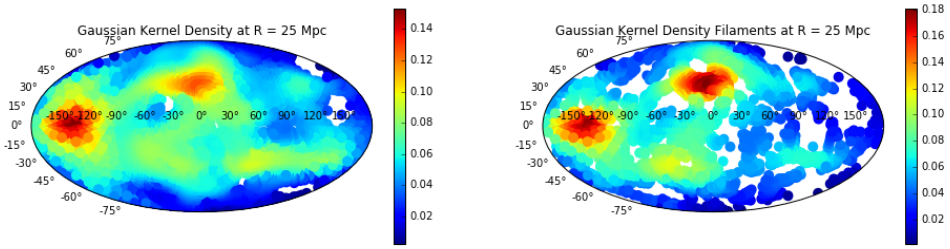


(e) Plot for the all particles (left) and the filaments (right) at a distance of 25 Mpc

Figure 42: plots of the surface density.